University of Leipzig
Faculty of Physics and Earth Sciences
Leipzig Institute for Meteorology

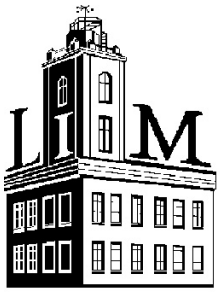

Implementation of a fluorescence channel in a multiwavelength lidar system to measure biological particles in the atmosphere

Master thesis

submitted by
Benedikt Gast
[redacted]
[redacted]

Summary

In this Master project, the MARTHA lidar system at TROPOS was upgraded by implementing a new fluorescence channel into both the near-range and far-range receivers. Two identical interference filters in tandem, centered at 466 nm and with a width of 44 nm, select a part of the fluorescence spectrum of fluorescing atmospheric particles and at the same time strongly suppress the elastic backscattering at the three laser wavelengths. A calculation approach for the fluorescence backscatter coefficient (β_{Fluo}), inspired by Veselovskii et al. (2020), was developed and further improved. As this approach uses a calibrated ratio of the fluorescence channel's signal and the nitrogen Raman signal, no reference height is needed to determine β_{Fluo}. Three measurement cases from summer and early autumn 2022 demonstrated the benefits of the new fluorescence information.

The measurements with the near-range channel showed that with this filter approach it is possible to detect the fluorescence of aerosol layers in the lower and middle troposphere. The analysis confirmed the size range of β_{Fluo} as four orders of magnitude lower than the elastic backscatter coefficients, as stated by Veselovskii et al. (2020). β_{Fluo} varied from $0.26 \times 10^{-4}\,\mathrm{Mm^{-1}\,sr^{-1}}$ for boundary-layer aerosol up to $1.45 \times 10^{-4}\,\mathrm{Mm^{-1}\,sr^{-1}}$ for a strong smoke layer. The fluorescence capacity (G_{F}) proved to be a useful tool to separate clouds from fluorescent aerosol. Moreover, when comparing two layers in combination with the associated elastic backscatter coefficients, G_{F} is a first indication of the fraction of fluorescent particles in the respective aerosol layer.

The far-range fluorescence channel was even capable of detecting thin smoke layers ($\beta_{1064} < 0.05\,\mathrm{Mm^{-1}\,sr^{-1}}$) in the upper troposphere and lower stratosphere up to 14 km height. Here, β_{Fluo} ranged between $1 \times 10^{-5}\,\mathrm{Mm^{-1}\,sr^{-1}}$ and $3.5 \times 10^{-4}\,\mathrm{Mm^{-1}\,sr^{-1}}$, with the low values belonging to dust (mixtures) and the higher values to smoke layers of wildfires. Particularly outstanding is that some of these fluorescent layers were not detectable in the range-corrected signals of the elastic channels.

A first statistical evaluation of the measurements with the far-range fluorescence channel indicated a fluorescence backscatter coefficient in the range of $2{-}6 \times 10^{-5}\,\mathrm{Mm^{-1}\,sr^{-1}}$ for most aerosol layers. The fluorescence capacity varied between 2×10^{-5} and 8×10^{-4}, and the smoke layers were characterized by significantly higher values than the rest. In contrast, the dust mixtures showed rather low values of G_{F}. This characteristic emphasizes the fluorescence capacity's potential for aerosol classification, particularly when combined with depolarization.

As the water-vapor channel was kept in the new MARTHA setup, the relative-humidity information could be used to show that most of the observed fluorescing aerosol layers were very dry. This anti-correlation of fluorescence and water vapor is an interesting issue to investigate and should therefore be considered further in future research.

Contents

1 Introduction

Climate change is increasing the number and intensity of wildfires (Xu et al., 2020). The global increase in average temperature (Gulev et al., 2021) and a precipitation shift to the winter season (Xu et al., 2020) increase the frequency, duration and intensity of heatwaves and droughts during the summer (Jones et al., 2020). The wildfire season is prolonged and the number of ignition sources raises (Xu et al., 2020). Intensive wildfires can produce large smoke plumes, which can be transported over larger distances and influence the radiation budget (via optical depth increase) and cloud cover (via aerosol-cloud interactions) even in remote areas. This connection corroborates the importance of studying wildfire aerosol in the atmosphere.
Pollen are an important factor for respiratory health. Besides causing allergies, recent studies suggest a relation of airborne pollen concentrations to an increase in cardiopulmonary and cardiovascular health outcomes (Nitschke et al., 2022; Bürgler et al., 2021). Atmospheric pollen concentrations have increased over the last decades, which may be attributed to the increased atmospheric CO_2 concentrations due to anthropogenic emissions (Ziello et al., 2012). Further, climate change has increased allergic diseases, e.g., due to a shift of the pollen season to earlier times in the year and an increased pollen production of wind-pollinated plants (Damialis et al., 2019). Thus, vertically and time-resolved pollen measurements − like a lidar can provide − may help to improve prevention of pollen-related health effects due to a better process understanding and improved forecasts.
Thus, both wildfire smoke and pollen are atmospheric aerosol types of increasing importance − not only because of their direct impact on us humans, but also because of their role in the changing climate of our planet. By influencing the Earth's radiation budget aerosol-cloud interactions play a key role in understanding and projecting climate change. Therefore, the aerosol type and properties have to be known outside and inside a cloud layer. Aerosol classification and the analysis of its optical properties is widely achieved by multiwavelength Raman lidar measurements of aerosol backscatter and extinction coefficients (Floutsi et al., 2022; Groß et al., 2013; Burton et al., 2012), although there are still some limitations. For example, smoke and volcanic sulfate in the stratosphere show similar properties and are therefore difficult to distinguish from each other. The same holds for pollen and mineral dust in the lower atmosphere. They are hard to distinguish in terms of optical properties. As wildfire smoke and pollen fluoresce, the detection of the laser-induced fluorescence can help in the distinction here. Veselovskii et al. (2020) implemented a fluorescence channel into a multiwavelength Raman lidar and presented a retrieval scheme for the fluorescence backscatter coefficient. They used this fluorescence channel to characterize the pollen load in northern France during the 2020 pollen season (Veselovskii et al., 2021). They also proposed a new inversion scheme for the retrieval of the particle number concentration from the fluorescence backscatter coefficient (Veselovskii et al., 2022a). In combination with the particle depolarization information, the fluorescence technique has proven to be a powerful tool for an improved aerosol classification by lidar (Veselovskii et al., 2022b).

The improved capability of lidar to identify and separate aerosol types by adding a fluorescence channel motivated this Master project. The main goal was to implement two new fluorescence channels in the **M**ultiwavelength **A**tmospheric **R**aman Lidar for **T**emperature, **H**umidity, and **A**erosol Profiling (MARTHA) at the Leibniz Institute for Tropospheric Research (TROPOS) in Leipzig and to realize first measurements.
This Master thesis is structured as follows: After this introduction, the basics of the lidar principle and the methodological background of aerosol type separation and aerosol fluorescence are outlined in Chapter 2. In Chapter 3, the determination of the aerosol fluorescence backscatter coefficient is explained. The lidar setup and the installation of the new fluorescence channels is presented in Chapter 4. In Chapter 5, first measurements with the upgraded MARTHA system are discussed. Starting with the observation of a single thin smoke layer below cirrus clouds, continuing with a strong smoke event and ending with hidden aerosol layers, the benefits of fluorescence measurements for aerosol analysis are illustrated. A summary in Chapter 6 completes the thesis.

2 Basics

The main topic approached here is the fluorescence induced by the scattering of the laser photons emitted by a lidar system. Subsequently, the separation of several aerosol types by means of measured aerosol properties and the physical process of fluorescence are explained. Finally, the optical features of a lidar system are described.

2.1 Lidar principle

The operation of a Raman lidar is described, e.g., in Whiteman et al. (1992). A pulsed laser beam is directed upward in such a way that it points vertically through the atmosphere. This laser beam propagates upward and interacts with aerosol particles and air molecules. This interaction happens through elastic and inelastic scattering as well as absorption. The backscattered radiation is detected and recorded as a function of the height. The height R itself is obtained from the photons' travel time t with $R = \frac{1}{2}\,c\,t$, where $c \approx 3 \times 10^8\,\mathrm{m\,s^{-1}}$ is the speed of light.
The goal is to get the scattering properties of the atmospheric particles. These are the particle backscatter coefficient (β_{par}) and the particle extinction coefficient (α_{par}). Extinction includes both scattering and absorption. From these optical properties one can then deduce the aerosol-characterizing quantities.

2.2 Lidar equation

The lidar equation quantifies the lidar return signal $P(R)$, which is received by the telescope from a distance R. It can be written as (Wandinger, 2005a)

$$P(R) = CG(R)\beta(R)T(R), \tag{2.1}$$

where the performance factor C of the lidar system and the range-dependent factor of the measurement geometry $G(R)$ are determined by the lidar setup. The backscatter coefficient $\beta(R)$ and the atmospheric transmission $T(R)$ at a distance R from the receiver depend on atmospheric properties and shall be investigated.
The system factor

$$C = P_0 \frac{c\tau}{2} A\eta \tag{2.2}$$

connects the average power of a laser pulse P_0 with the pulse length τ, the speed of light c, the telescope area A and the system efficiency η (Wandinger, 2005a).
The lidar geometry is illustrated in Fig. 2.1. The geometric factor

$$G(R) = \frac{O(R)}{R^2} \tag{2.3}$$

is defined as the quotient of the laser-beam receiver-field-of-view overlap function $O(R)$ and the squared distance R^2. The overlap function accounts for the fact that at short

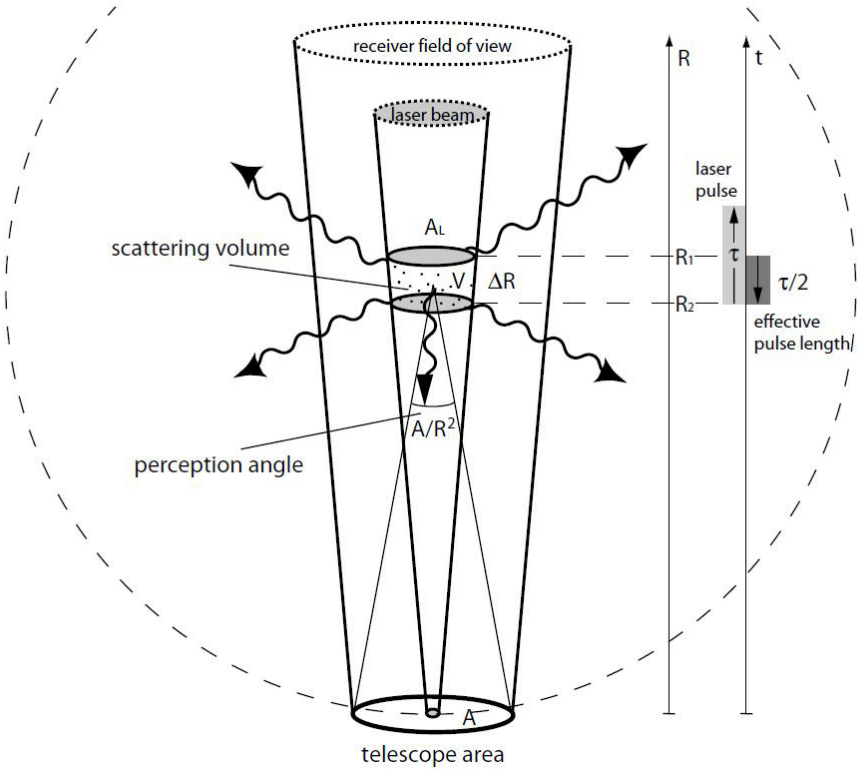

Figure 2.1: Illustration of the lidar geometry (Wandinger, 2005a).

distances only a part of the actual return signal is measured as only a part of the laser beam can be imaged onto the detector. It is equal to zero at the lidar and equal to one at the height, from which on the entire laser beam is imaged onto the detector. The lidar signal decreases quadratically with the distance (R^{-2}) because the telescope area A can be seen as a part of a sphere's surface with the radius R enclosing the scattering volume (cf. Fig. 2.1) (Wandinger, 2005a).
The wavelength-dependent backscatter coefficient $\beta(R, \lambda_0)$ describes the amount of light that is scattered in backward direction (180° scattering angle) at the laser wavelength λ_0. By summing over all kinds of scattering particles j, it is defined as

$$\beta(R, \lambda_0) = \sum_j N_j(R) \frac{\mathrm{d}\sigma_{j,\mathrm{sca}}}{\mathrm{d}\Omega}(\pi, \lambda_0), \tag{2.4}$$

with N_j the concentration of scattering particles of the kind j in the illuminated volume and the scattering cross section $\frac{\mathrm{d}\sigma_{j,\mathrm{sca}}}{\mathrm{d}\Omega}(\pi, \lambda_0)$ in backward direction at wavelength λ_0. Since scattering in the atmosphere occurs by molecules and aerosol particles, the backscatter coefficient can also be written as

$$\beta(R, \lambda_0) = \beta_{\mathrm{mol}}(R, \lambda_0) + \beta_{\mathrm{par}}(R, \lambda_0), \tag{2.5}$$

with the indices mol for the molecular and par for the particulate component (Wandinger, 2005a).
The transmission term

$$T^2(R,\lambda_0) = \exp\left[-2\int_0^R \alpha(r,\lambda_0)\mathrm{d}r\right] \tag{2.6}$$

describes the attenuation of the laser light on its way through the atmosphere and can take values between 0 and 1. The extinction coefficient

$$\alpha(R,\lambda_0) = \sum_j N_j(R)\sigma_{j,\mathrm{ext}}(\lambda_0) \tag{2.7}$$

or

$$\alpha(R,\lambda_0) = \alpha_{\mathrm{mol}}(R,\lambda_0) + \alpha_{\mathrm{par}}(R,\lambda_0) \tag{2.8}$$

is defined in analogy to Eq. (2.4) as the product of N_j and the extinction cross section $\sigma_{j,\mathrm{ext}}$ for each kind j of scattering particles, and it comprises of a molecular and a particulate component in analogy to Eq. (2.5) (Wandinger, 2005a).
With these detailed notations of its four terms, the lidar equation can now be written in the final form:

$$P(R,\lambda_0) = P_0\frac{c\tau}{2}A\eta\frac{O(R)}{R^2}\beta(R,\lambda_0)\exp\left[-2\int_0^R \alpha(r,\lambda_0)\mathrm{d}r\right]. \tag{2.9}$$

If a lidar system is equipped with a Raman channel to detect also the inelastic scattering at air molecules, the lidar equation for the return signal in the nitrogen Raman channel at wavelength λ_{Ra} takes the form (Wandinger, 2005b):

$$P(R,\lambda_{\mathrm{Ra}}) = P_0\frac{c\tau}{2}A\eta\frac{O(R)}{R^2}\beta_{\mathrm{N_2}}(R,\lambda_{\mathrm{Ra}})\exp\left[-\int_0^R [\alpha(r,\lambda_0)+\alpha(r,\lambda_{\mathrm{Ra}})]\mathrm{d}r\right], \tag{2.10}$$

or in more detail:

$$\begin{aligned} P(R,\lambda_{\mathrm{Ra}}) &= P_0\frac{c\tau}{2}A\eta\frac{O(R)}{R^2}\beta_{\mathrm{N_2}}(R,\lambda_{\mathrm{Ra}}) \\ &\quad\times\exp\left[-\int_0^R [\alpha_{\mathrm{mol}}(r,\lambda_0)+\alpha_{\mathrm{par}}(r,\lambda_0)+\alpha_{\mathrm{mol}}(r,\lambda_{\mathrm{Ra}})+\alpha_{\mathrm{par}}(r,\lambda_{\mathrm{Ra}})]\mathrm{d}r\right] \\ &=: C_{\mathrm{R}}\frac{O(R)}{R^2}\beta_{\mathrm{R}}T_{\mathrm{L}}T_{\mathrm{R}} =: P_{\mathrm{R}}, \end{aligned} \tag{2.11}$$

where $T_{\mathrm{L}} := T(R,\lambda_0)$ and $T_{\mathrm{R}} := \exp\left[-\int_0^R[\alpha_{\mathrm{mol}}(r,\lambda_{\mathrm{Ra}})+\alpha_{\mathrm{par}}(r,\lambda_{\mathrm{Ra}})]\mathrm{d}r\right]$.
In the following, only an excitation wavelength of 355 nm and thus the nitrogen Raman signal at 387 nm will be used to derive the fluorescence of atmospheric aerosol particles. The determination of the fluorescence backscatter coefficient is introduced in Chapter 3. Two methods for solving the lidar equation are described in Appendix A.

2.3 Intensive aerosol optical properties

In this section, the intensive, i.e., concentration-independent, aerosol-characterizing optical properties (lidar ratio, depolarization ratio and color ratio) are introduced.

2.3.1 Lidar ratio

The lidar ratio S is defined as

$$S(R, \lambda_0) = \frac{\alpha_{\text{par}}(R, \lambda_0)}{\beta_{\text{par}}(R, \lambda_0)}, \tag{2.12}$$

the ratio of the particle extinction to the particle backscatter coefficient, and it follows their height and wavelength dependence. On the one hand, it depends on the form of the phase function of the particles, related to the shape and size of them. On the other hand, it also depends strongly on the absorption efficiency of the particles, which might considerably increase the extinction coefficient, making the lidar ratio large in the case of highly absorbing particles (Ansmann and Müller, 2005).

2.3.2 Depolarization ratio

The second important aerosol property is the depolarization ratio. The principle of depolarization is illustrated in Fig. 2.2(a). The light emitted by the laser is completely linearly polarized (indicated by the green horizontal arrows in Fig. 2.2(a)). When being backscattered in the atmosphere, the light can change its polarization, and this change is closely related to the particle shape. The particle linear depolarization ratio is defined as (Freudenthaler et al., 2009):

$$\delta(R, \lambda_0) = \frac{\beta^{\perp}_{\text{par}}(R, \lambda_0)}{\beta^{\parallel}_{\text{par}}(R, \lambda_0)}, \tag{2.13}$$

with $\beta^{\parallel}_{\text{par}}(R, \lambda_0)$ the parallel- and $\beta^{\perp}_{\text{par}}(R, \lambda_0)$ the cross-polarized components of the particle

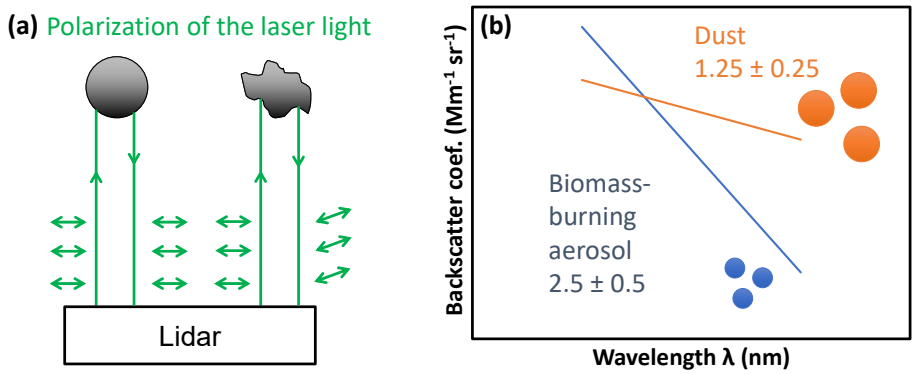

Figure 2.2: (a) Illustration of the principle of depolarization. (b) Wavelength dependence of the particle backscatter coefficients for dust and BBA. Color ratio values for $\lambda_1 = 532\,\text{nm}$ and $\lambda_2 = 1064\,\text{nm}$ are given with their uncertainties.

backscatter coefficient. Spherical particles do not change the polarization state during the backscattering process. The backscattered radiation is still linearly polarized. However, non-spherical particles change the polarization state, i.e., they depolarize laser light. This change is indicated by a light tilt of the green arrows in Fig. 2.2(a) after the scattering process. Thus, the depolarization ratio is an indicator for non-sphericity of the particles. It shows low values for spherical particles like pollution and higher values for non-spherical particles such as desert dust (Haarig et al., 2017; Ohneiser et al., 2020; Haarig et al., 2022).

2.3.3 Color ratio

Finally, a third practical quantity is the color ratio (CR). It describes the spectral behavior of the backscatter coefficient by using two different wavelengths. It is defined as

$$\chi(R) = \frac{\beta(R, \lambda_1)}{\beta(R, \lambda_2)}, \tag{2.14}$$

the ratio of the particle backscatter coefficients at the wavelengths λ_1 and λ_2. Often the color ratio of $\lambda_1 = 532\,\text{nm}$ and $\lambda_2 = 1064\,\text{nm}$ is used (Burton et al., 2012; Kanngiesser and Kahnert, 2019).
As an example, the wavelength dependence of the backscatter coefficient for dust and biomass-burning aerosol (BBA) is shown in Fig. 2.2(b). Dust shows only a weak wavelength dependence, resulting in a color ratio of around 1.25 (Zhang et al., 2019; Burton et al., 2012). In contrast, the backscattering of biomass-burning aerosol strongly decreases with increasing wavelength, meaning a higher color ratio of around 2.5 (Burton et al., 2012).

2.4 Aerosol type separation

Classification schemes, based on the previously mentioned aerosol-characterizing quantities, have emerged during the last decades. Floutsi et al. (2022); Burton et al. (2012); Groß et al. (2013), e.g., analyzed the typical values of intensive aerosol optical properties for several types of aerosols. Their usage for the aerosol typing is discussed in this section. For this purpose, we distinguish between high, medium and low values for each quantity for the different aerosol types. The results are summarized in Tab. 2.1.
The largest differences for different aerosol types are found in the depolarization ratio. Fig. 2.3 shows characteristic values in terms of particle linear depolarization ratio and lidar ratio at 532 nm for various atmospheric aerosol types. The highest depolarization ratio is found for mineral dust and its mixtures with 20−35 % (Freudenthaler et al., 2009; Groß et al., 2011; Veselovskii et al., 2016; Hu et al., 2020; Haarig et al., 2022; Floutsi et al., 2022). Fresh (African) mixtures of biomass-burning aerosol and dust lead to a moderate level of depolarization (8−26 %) (Groß et al., 2011; Ohneiser et al., 2020). Anthropogenic pollution aerosols, aged (Canadian) BBA and marine aerosol show similar values of the depolarization ratio in the single-digit percentage range (Groß et al., 2013; Haarig et al.,

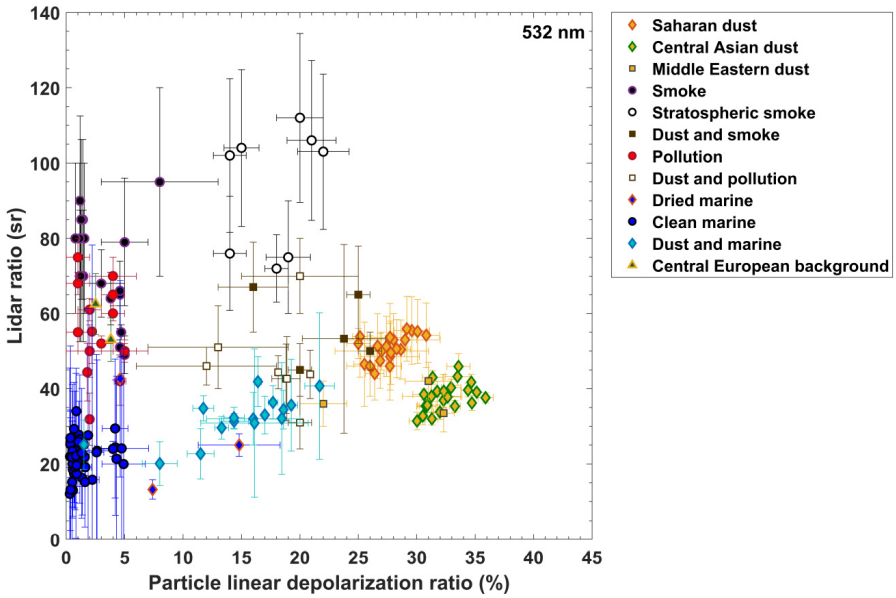

Figure 2.3: Characteristic values of lidar ratio and particle linear depolarization ratio at 532 nm for various atmospheric aerosol types (Floutsi et al., 2022).

2018; Floutsi et al., 2022).

Volcanic ash shows high depolarization ratios (Sassen et al., 2007; Ansmann et al., 2010; Groß et al., 2012). Thus, mineral dust, volcanic ash and fresh BBA show quite unique values of the depolarization ratio, but they vary within a certain range. For an efficient separation, as well as for the types with low depolarization, more information is needed. Therefore, one can have a look at the lidar ratio next, where all values are given at 532 nm. Clearly, marine aerosols show very low values of the lidar ratio of around 15−25 sr (Floutsi et al., 2022; Groß et al., 2011) compared to the other aerosol types. Urban haze exhibits 532 nm lidar ratios of 35−65 sr (Mattis et al., 2004), absorbing anthropogenic pollution of around 65−75 sr (Mattis et al., 2004). For BBA, the 532 nm lidar ratio shows the highest values in the range of 65−100 sr (Haarig et al., 2018; Ohneiser et al., 2020, 2021; Floutsi et al., 2022).

The color ratio may provide further clarity. For most aerosol types, the 532 to 1064 nm color ratio is quite similar, ranging from 1 to 2 (Burton et al., 2012; Groß et al., 2013). Only anthropogenic pollution and BBA show higher values. BBA displays a wide spread in CR from 1.5−3 (Burton et al., 2012) with large uncertainties. For anthropogenic pollution, the CR values are around 1.5−2.5 (Burton et al., 2012). Thus, also the CR ranges are quite overlapping for these two aerosol types, making the distinction difficult. When we look at Tab. 2.1, also volcanic sulfate shows similar properties as smoke and pollution aerosol, although the lidar ratio is a bit smaller. The separation of smoke and volcanic sulfate is often a problem for the proper classification of stratospheric aerosol layers. Both aerosol types are found in the accumulation mode and exhibit typically low depolarization ratios when occurring in stratospheric aerosols layers. The lidar ratio is not of much help either, as it varies widely depending on the particular measurement case. In general, all aerosol types have their characteristic fingerprints, but they vary within a certain range.

Table 2.1: Typical magnitude of the aerosol-characterizing properties and fluorescence for various aerosol types. It is only distinguished between high (h), medium (m) and low (l) values.

	Depolarization at 532 nm	Lidar ratio at 532 nm	Color ratio 532/1064 nm	Fluorescence (444−488 nm)
Dust	high	medium	low	low
Marine	low	low	low	?
Smoke	l - m	high	m - h	high
Anthropogenic pollution	low	medium	high	low
Absorbing pollution	low	high	high	low
Volcanic ash	high	medium	low	low
Volcanic sulfate (low + moderate eruptions)	low	medium	high	low
Volcanic sulfate (major eruptions)	low	low	low	low
Pollen	m - h	medium	low	high

Hence, another measured quantity would provide more unambiguity. Here, the fluorescence may help.
Table 2.1 shows that smoke and pollen are fluorescent, while the other types are not. Only for marine aerosol, it is not completely clear as it could contain small portions of biological material. Therefore, the question mark was put in the table. But if marine aerosol would fluoresce, its fluorescence would be much weaker than for smoke and pollen. As smoke is fluorescent, while anthropogenic pollution and volcanic sulfates are not, the latter two types can be easily separated from smoke.
Another example of classification difficulties is the separation of dust and pollen. Both show similar aerosol optical properties (cf. Tab. 2.1) and cannot be separated without any additional information. But pollen are fluorescing while dust is not. Thus, pollen and dust can be separated by using fluorescence as well.
As we see, fluorescence measurements could greatly improve aerosol classification. That is the motivation, why we want to implement a fluorescence channel into the MARTHA system. But beforehand the optical phenomenon fluorescence has to be clarified, what is done in the next section.

2.5 Fluorescence

Fluorescence is the emission of light by a substance that has absorbed electromagnetic radiation at a shorter wavelength before. The substances that are fluorescent are called fluorophores.
The fluorescence process is illustrated in Fig. 2.4. Due to the absorption of electromagnetic radiation of the wavelength λ_1 an electron transition from the ground state S_0 to a higher energy level S_2 takes place. The fluorophore is excited. The excited state exists only for a short time ($\sim$ 1−10 ns). During this time span, the fluorophore is subject to some

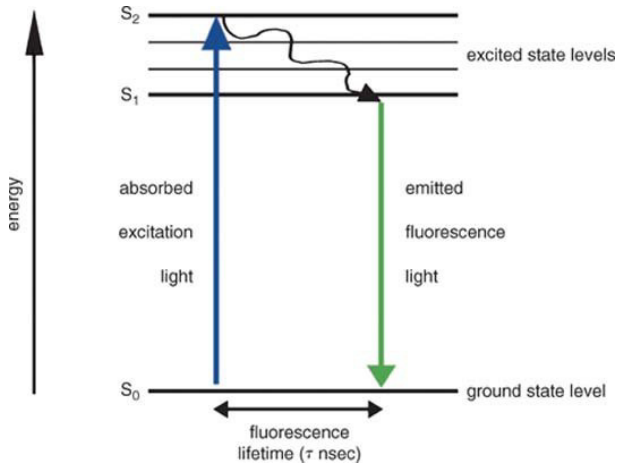

Figure 2.4: Energy states of a molecule during the fluorescence process, illustrated in a Jablonski diagram (Lleres et al., 2007).

changes and interactions with its molecular environment. This process is called internal conversion (Lakowicz, 2006).
As a result, a part of the energy, which was absorbed before for the transition to S_2, is already dissipated, i.e., the molecule is now at a lower energy state S_1. From this energy level, the fluorescence emission originates in the following. Returning to the ground state S_0 leads to an emission of a photon with lower energy (and thus longer wavelength λ_2) than the absorbed photon (i.e., $\lambda_2 > \lambda_1$). The energy difference is called 'Stokes shift' (Lakowicz, 2006).

2.5.1 Fluorescence spectra of pollen

In several studies, measurements of pollen fluorescence spectra were conducted for different excitation wavelengths (cf. Figs. 2.5−2.7). Saito et al. (2018) and Zhang et al. (2021)

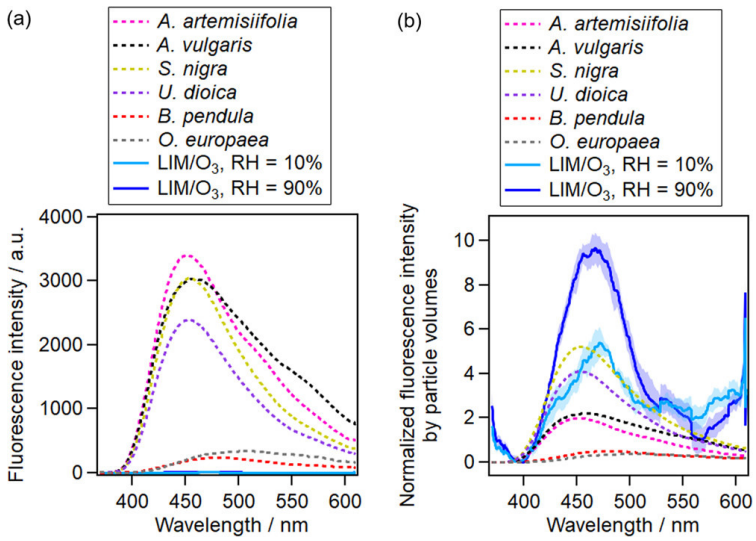

Figure 2.5: Pollen fluorescence spectra of mainly Asian pollen species for an excitation wavelength of 355 nm (Zhang et al., 2021).

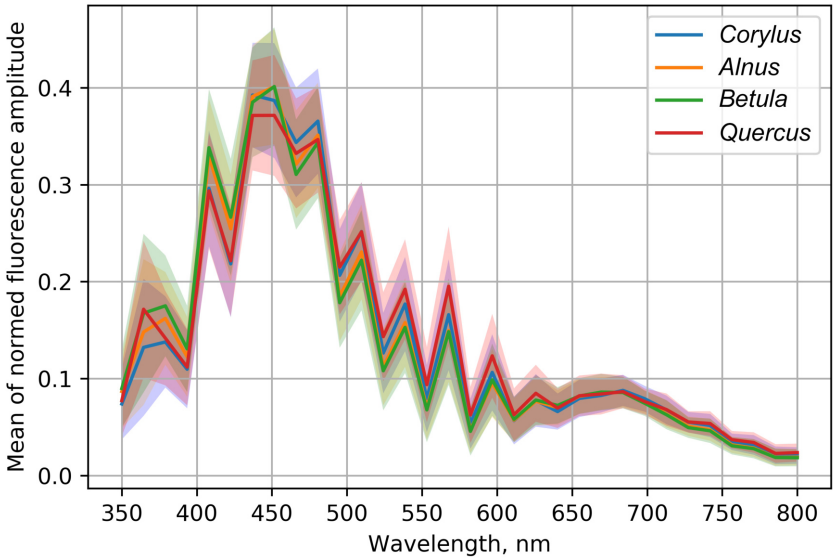

Figure 2.6: Fluorescence spectra of hazel, alder, birch and oak pollen for an excitation wavelength of 320 nm (Šaulienė et al., 2019).

measured fluorescence spectra at 355 nm, one of the laser wavelengths of the MARTHA system. Mainly Asian tree species were examined and, in general, exhibited a peak in fluorescence intensity at around 460 nm (Saito et al., 2018; Zhang et al., 2021). For more common European species, literature provides only measurements at slightly shifted excitation wavelengths. All in all, Pan et al. (2011); Pan (2015) (351 nm) and Šaulienė et al. (2019) (320 nm excitation) confirmed that the maximum fluorescence intensity for pollen is to be found in a wavelength range from 440 nm to 480 nm.

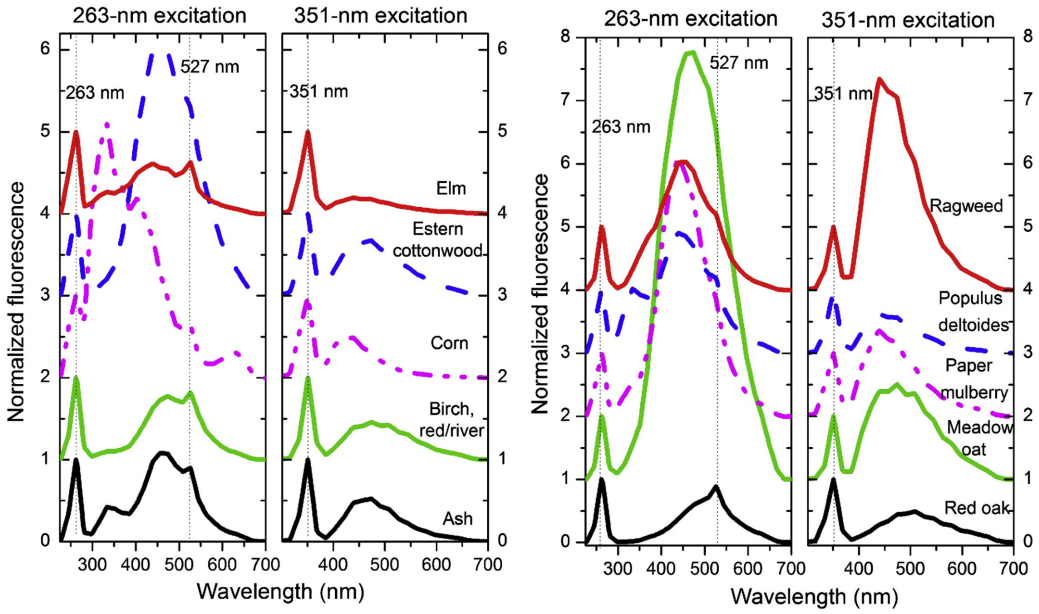

Figure 2.7: Pollen fluorescence spectra of elm, cotton, corn, birch, ash, ragweed, poplar, paper mulberry, meadow oat and red oak for excitation wavelengths of 263 and 351 nm (Pan et al., 2011).

2.5.2 Fluorescence spectra of smoke

For wildfire smoke, data are sparse. Reichardt et al. (2018) measured fluorescence spectra of BBA for an excitation wavelength of 355 nm using the Raman lidar RAMSES of the German Meteorological Service (Deutscher Wetterdienst, DWD) in Lindenberg. They measured the fluorescence spectrum during local Easter bonfires (dashed black line in Fig. 2.8) and compared it to an undisturbed boundary layer (solid black line in Fig. 2.8). The smoke of the Easter bonfires shows a local maximum in fluorescence intensity at around 540 nm, i.e., at larger wavelengths than the pollen. In this wavelength range, also the difference to the spectrum for an undisturbed boundary layer (black solid line) is greatest. Fig. 2.8 also shows the fluorescence spectra for three smoke layers measured at 3−7 km height in September 2015 and September 2016. Those smoke layers exhibit a local maximum in fluorescence intensity in the wavelength range from 480 to 540 nm. The spectrum on 6 September 2016 (red curve) even closely resembles the spectrum of the boundary layer during the Easter bonfires.
Veselovskii et al. (2020) added a single fluorescence channel to a multiwavelength Raman lidar system at Lille. Even if they did not measure spectra, they showed that the spectral range from 440−490 nm is suitable for observing fluorescence from both pollen and wildfire smoke (Veselovskii et al., 2020, 2021). Thus, the same wavelength range was used in this Master project for the implementation of a new fluorescence channel into the MARTHA system.

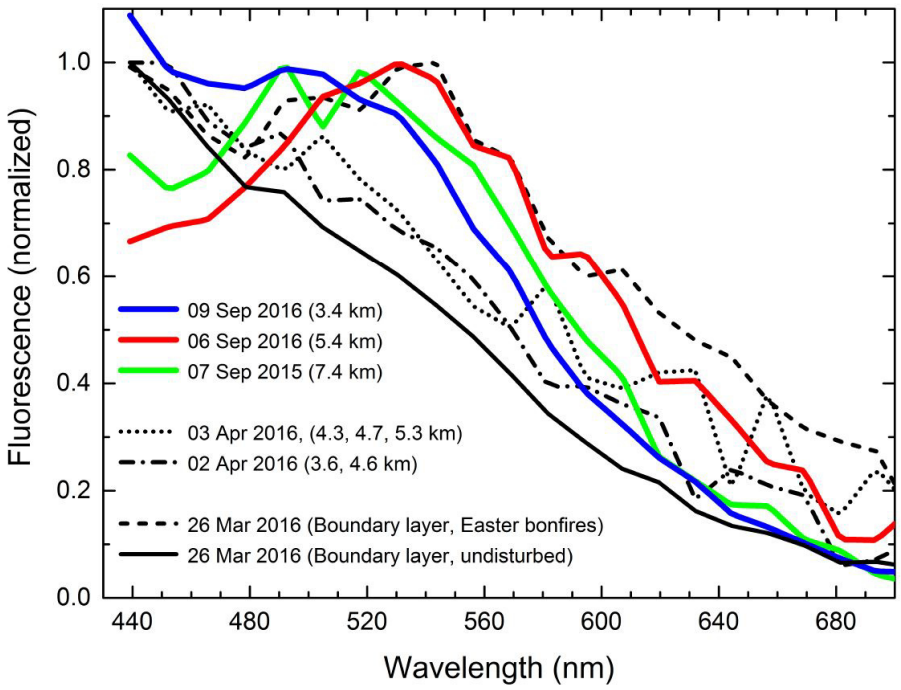

Figure 2.8: Normalized fluorescence spectra of free-troposphere aerosol for measurements on 9 September 2016 (blue) and 7 September 2015 (green). Typical fluorescence spectra of the boundary layer are shown for comparison: undisturbed (solid black curve) and with smoke of Easter bonfires in March 2016 (dashed black curve) (Reichardt et al., 2018).

3 Determination of the aerosol fluorescence backscatter coefficient

The approach for the determination of the fluorescence backscatter coefficient, used in this thesis, was inspired by the method proposed by Veselovskii et al. (2020). Starting from the lidar equation (Eq. (2.9)), the fluorescence signal caused by aerosol fluorescence can be described as

$$\begin{aligned} P_{\mathrm{F}} = \frac{O(R)}{R^2} T_{\mathrm{L}} \int_{\lambda_{\min}}^{\lambda_{\max}} C_{\mathrm{F}}(\lambda) \int_{s_{\min}}^{s_{\max}} \frac{\mathrm{d}N(s)}{\mathrm{d}s} \frac{\mathrm{d}\sigma_{\mathrm{F}}}{\mathrm{d}\lambda}(\lambda, s) \\ \times \exp\left[- \int_0^R [\alpha_{\mathrm{mol}}(r,\lambda) + \alpha_{\mathrm{par}}(r,\lambda)] \mathrm{d}r \right] \mathrm{d}s \mathrm{d}\lambda, \end{aligned} \tag{3.15}$$

with the notation $T_{\mathrm{L}} \coloneqq T(R, \lambda_0)$ for the atmospheric transmission at the laser wavelength (on the way up to the scattering event). The fluorescence spectrum emitted by atmospheric particles extends over a broad spectral range, as it was shown in Section 2.5. Thus, the integral $\int_{\lambda_{\min}}^{\lambda_{\max}} [...] \, \mathrm{d}\lambda$ accounts for the wavelength dependence of the fluorescence as well as the molecular and particle extinction coefficients inside the transmission band $[\lambda_{\min}, \lambda_{\max}]$ of the used interference filter in the fluorescence channel. Additionally, the particle size distribution $\frac{\mathrm{d}N(s)}{\mathrm{d}s}$ of particles with radius between s and $s + \mathrm{d}s$ has to be considered, as the spectral differential fluorescence cross section $\frac{\mathrm{d}\sigma_{\mathrm{F}}}{\mathrm{d}\lambda}(\lambda, s)$ depends on the size of the fluorescing particles. $C_{\mathrm{F}}(\lambda) = P_0 \frac{c\tau}{2} A \eta_{\mathrm{F}}(\lambda)$ is the lidar calibration constant for the fluorescence channel. Its main wavelength-dependent quantity is the optical efficiency $\eta_{\mathrm{F}}(\lambda)$, as it is influenced by the interference filter's transmission curve. In this Master project, an interference filter with a transmission band from 444 to 488 nm and a central wavelength of 466 nm was used (see Section 4.3). For the filter width ($\lambda_{\max} - \lambda_{\min} = 44$ nm) in the fluorescence channel, the atmospheric transmission for its signal,

$$T_{\mathrm{F}}(\lambda) = \exp\left[- \int_0^R [\alpha_{\mathrm{mol}}(r,\lambda) + \alpha_{\mathrm{par}}(r,\lambda)] \mathrm{d}r \right], \tag{3.16}$$

can be considered simplified at the central wavelength $\lambda_{\mathrm{F}} = 466$ nm of the interference filter: $T_{\mathrm{F}}(\lambda) = T_{\mathrm{F}}(\lambda_{\mathrm{F}}) =: T_{\mathrm{F}}$. Since the transmission of the interference filter used is rather constant over the filter spectral bandwidth, the same can be assumed for C_{F}. With the definition of the fluorescence backscatter coefficient β_{F} (Veselovskii et al., 2020),

$$\beta_{\mathrm{F}} = \int_{s_{\min}}^{s_{\max}} \frac{\mathrm{d}N(s)}{\mathrm{d}s} \sigma_{\mathrm{F}}(s) \mathrm{d}s = \int_{\lambda_{\min}}^{\lambda_{\max}} \int_{s_{\min}}^{s_{\max}} \frac{\mathrm{d}N(s)}{\mathrm{d}s} \frac{\mathrm{d}\sigma_{\mathrm{F}}}{\mathrm{d}\lambda}(\lambda, s) \mathrm{d}s \mathrm{d}\lambda, \tag{3.17}$$

Eq. (3.15) can be rewritten as

$$P_{\mathrm{F}} = \frac{O(R)}{R^2} C_{\mathrm{F}} \beta_{\mathrm{F}} T_{\mathrm{F}} T_{\mathrm{L}}. \tag{3.18}$$

Building the ratio of the fluorescence and the nitrogen Raman signal (i.e., dividing Eq. (3.18) by Eq. (2.11)) and rearranging for the fluorescence backscatter coefficient, one obtains (Veselovskii et al., 2020):

$$\beta_{\mathrm{F}} = \frac{P_{\mathrm{F}}}{P_{\mathrm{R}}} \beta_{\mathrm{R}} \frac{T_{\mathrm{R}}}{T_{\mathrm{F}}} \frac{C_{\mathrm{R}}}{C_{\mathrm{F}}}. \tag{3.19}$$

The signal ratio $P_{\mathrm{F}}/P_{\mathrm{R}}$ is measured. The calculation of the ratio $T_{\mathrm{R}}/T_{\mathrm{F}}$ of atmospheric transmissions at λ_{Ra} and λ_{F} is done similar to the calculation of the transmission ratio of the water-vapor and nitrogen Raman channels for water-vapor measurements as described by Whiteman et al. (2006). At this stage of the project, the influence of the wavelength dependence of the particle extinction coefficient is neglected, i.e., it is assumed that $\alpha_{\mathrm{par}}(r, \lambda_{\mathrm{F}}) = \alpha_{\mathrm{par}}(r, \lambda_{\mathrm{Ra}})$. Thus, $T_{\mathrm{R}}/T_{\mathrm{F}}$ is calculated from the molecular extinction coefficients, which are obtained from Global Data Assimilation System (GDAS) model profiles of temperature and pressure. The consideration of the wavelength dependence of the particle extinction coefficient for the transmission ratio calculation is ongoing work.
As the laser power, pulse length and telescope area are the same for the Raman and fluorescence signals, the lidar calibration constant ratio $C_{\mathrm{R}}/C_{\mathrm{F}}$ simplifies to the ratio of the respective optical system efficiencies $\eta_{\mathrm{R}}/\eta_{\mathrm{F}}$. Its value depends on the measuring setup (near-range (NR) or far-range (FR) channel) and is described further in Section 4.4.3.
The Raman backscatter coefficient of nitrogen molecules β_{R} is defined by the molecule number density $N_{\mathrm{N_2}}(R)$ of nitrogen and the differential Raman cross section in backward direction $\frac{\mathrm{d}\sigma_{\mathrm{N_2}}}{\mathrm{d}\Omega}(\pi, \lambda_{\mathrm{Ra}})$ (Wandinger, 2005b):

$$\beta_{\mathrm{R}} = N_{\mathrm{N_2}}(R) \frac{\mathrm{d}\sigma_{\mathrm{N_2}}}{\mathrm{d}\Omega}(\pi, \lambda_{\mathrm{Ra}}). \tag{3.20}$$

With the volume concentration of nitrogen in the atmosphere, $N_{\mathrm{N_2}}(R)$ can be expressed in terms of the number concentration of air molecules N_{mol}:

$$N_{\mathrm{N_2}}(R) = 0.78 N_{\mathrm{mol}}(R) = 0.78 \frac{\beta_{\mathrm{mol}}(R, \lambda_0)}{\frac{\mathrm{d}\sigma_{\mathrm{mol}}}{\mathrm{d}\Omega}(\pi, \lambda_0)}. \tag{3.21}$$

$\beta_{\mathrm{mol}}(R, \lambda_0)$ is the molecular backscatter coefficient and $\frac{\mathrm{d}\sigma_{\mathrm{mol}}}{\mathrm{d}\Omega}(\pi, \lambda_0)$ the Rayleigh backscatter differential cross section. With the abbreviation forms $D_{\mathrm{R}} \coloneqq \frac{\mathrm{d}\sigma_{\mathrm{N_2}}}{\mathrm{d}\Omega}(\pi, \lambda_{\mathrm{Ra}})$ and $D_{\mathrm{mol}} \coloneqq \frac{\mathrm{d}\sigma_{\mathrm{mol}}}{\mathrm{d}\Omega}(\pi, \lambda_0)$, Eq. (3.20) can then be written in the following form:

$$\beta_{\mathrm{R}} = 0.78 \frac{D_{\mathrm{R}}}{D_{\mathrm{mol}}} \beta_{\mathrm{mol}}(R, \lambda_0). \tag{3.22}$$

Inserting Eq. (3.22) into Eq. (3.19) leads to the final equation for the fluorescence backscatter coefficient:

$$\beta_{\mathrm{F}} = \frac{P_{\mathrm{F}}}{P_{\mathrm{R}}} 0.78 \beta_{\mathrm{mol}}(R, \lambda_0) \frac{D_{\mathrm{R}}}{D_{\mathrm{mol}}} \frac{T_{\mathrm{R}}}{T_{\mathrm{F}}} \frac{\eta_{\mathrm{R}}}{\eta_{\mathrm{F}}}. \tag{3.23}$$

Using the calculation method according to Adam (2009), values of $D^*_{\mathrm{R}} = 2.7344 \times 10^{-34}\,\mathrm{m^2\,sr^{-1}}$ and $D_{\mathrm{mol}} = 3.10875 \times 10^{-31}\,\mathrm{m^2\,sr^{-1}}$ are obtained for the nitrogen vibrational-rotational backscatter differential cross section and the Rayleigh backscatter differential cross section, respectively. But, depending on the width of the 387 nm filter, only a certain fraction p_{filter} of D^*_{R} reaches the detector in the nitrogen Raman channel ($D_{\mathrm{R}} = p_{\mathrm{filter}} D^*_{\mathrm{R}}$). For the 387 nm near-range channel with a filter width of 0.6 nm, a fraction of $p^{\mathrm{NR}}_{\mathrm{filter}} = 0.35$ was obtained. The wider interference filter in the far-range channel still sees about 95 % of D^*_{R} ($p^{\mathrm{NR}}_{\mathrm{filter}} = 0.95$). The ratio results in $\frac{D_{\mathrm{R}}}{D_{\mathrm{mol}}} = \frac{p_{\mathrm{filter}} D^*_{\mathrm{R}}}{D_{\mathrm{mol}}} = p_{\mathrm{filter}} \times 8.7959 \times 10^{-4}$. $\beta_{\mathrm{mol}}(R, \lambda_0)$ is also obtained from GDAS model profiles of temperature and pressure.

4 Implementation of two new fluorescence channels into MARTHA

A major part of this Master project was the design and technical implementation of the new fluorescence channels in the MARTHA system. This chapter describes the old MARTHA setup without fluorescence channels. Afterwards, the implementation process is presented and some technical details are explained.

4.1 MARTHA setup before the implementation of the fluorescence channels

In this work, the main measurement system was the stationary lidar system MARTHA, which is located at TROPOS in Leipzig (51.35° N, 12.43° E). MARTHA was part of the **E**uropean **Aer**osol **R**esearch **Li**dar **Net**work (EARLINET) and was used within this framework for long-term aerosol measurements. Besides, it is used as a laboratory for the development and testing of new lidar techniques (e.g., Schmidt et al. (2013); Jimenez et al. (2020)).
A pulsed Nd:YAG laser emits a total pulse energy of 1.4 J at a repetition rate of 30 Hz and wavelengths of 1064, 532 and 355 nm. A magnification with a factor of 15 is realized by a beam expander before the laser beam is directed to the atmosphere. The far-range telescope, which is aligned coaxial, has a diameter of 80 cm. The near-range telescope is 20 cm in diameter (Schmidt et al., 2013).
The collected backscattered radiation is transmitted to the receiver unit, where it is analyzed spectrally. The separation of the radiation according to wavelength is realized by dichroic beam splitters, which reflect a part of the radiation into the various detection channels. The setup of the MARTHA receiving unit before the implementation of the fluorescence channels is sketched in Fig. 4.1.
The return signals from elastic Rayleigh backscattering are collected in the 355, 532 and 1064 nm channels. The 387 and 607 nm channels detect radiation that is generated by inelastic Raman scattering at nitrogen molecules. The water-vapor mixing ratio is measured using the 407 nm detection channel, and from the mixing ratio the relative humidity is derived. The 532 nm channels (pp - parallel polarized and cp - cross polarized) allow the derivation of a depolarization ratio. Temperature profiles can be obtained via the pure rotational Raman channels (355.4 and 356.3 nm in Fig. 4.1) (Schmidt et al., 2013).
In this Master project, a new fluorescence channel was implemented into the MARTHA system. Due to logistical reasons, it was firstly implemented into the near-range and later into the far-range receiver. A more detailed description of the implementation is given in the following sections.

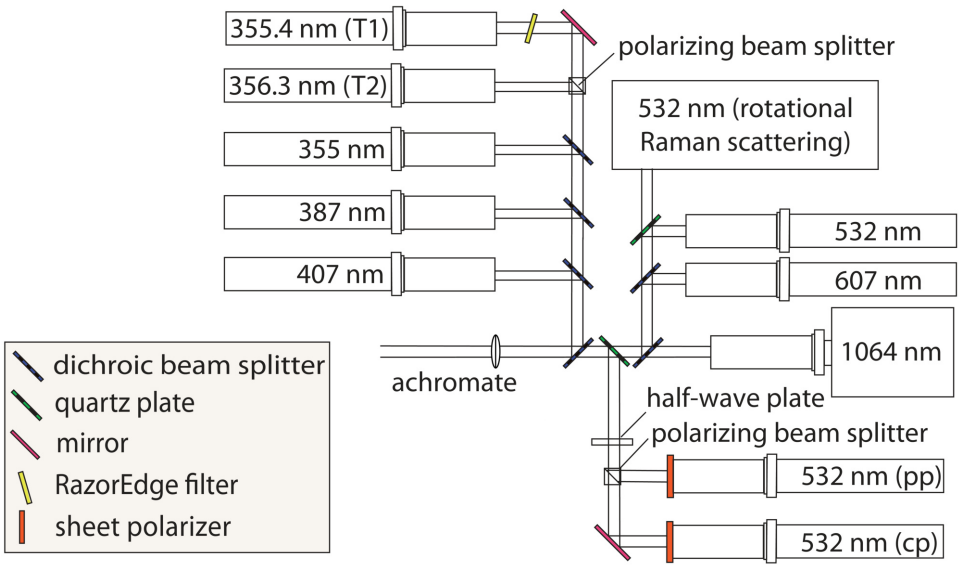

Figure 4.1: Setup of the MARTHA far-range receiver before the implementation of the fluorescence channel.

4.2 Design of the new fluorescence channels

At the beginning of the project, a decision had to be made which measurement approach should be used to realize lidar fluorescence measurements at TROPOS. A spectrometer approach as used by Reichardt et al. (2018) gives a better spectral resolution than a single detection channel with an interference filter of certain width. The detailed spectral information might allow a clearer distinction between fluorescing aerosol types (e.g., between pollen and wildfire smoke). But in the end, this spectrometer approach is quite costly and sophisticated.

Furthermore, Veselovskii et al. (2020) showed that, in combination with other lidar quantities, an aerosol classification is very well possible even with a single-interference-filter approach. Such a single fluorescence channel is easier to realize and delivers a stronger signal due to its comparably large filter width, which makes the signal better distinguishable from background noise. And as this was the first try of lidar fluorescence measurements at TROPOS, it was decided to start with a filter approach, which was inspired by the results from Veselovskii et al. (2020).

For the decision on the spectral range of the interference filter, typical fluorescence spectra for pollen and wildfire smoke were considered. As it was shown in Section 2.5, the maximum fluorescence intensity for pollen is found in a wavelength range from 440 nm to 480 nm and also biomass-burning aerosol exhibits a pronounced level of fluorescence intensity in this spectral range, although the maximum is at somewhat larger wavelengths. Consequently, it was decided to use a similar interference filter as Veselovskii et al. (2020), which has its transmission band in this wavelength range, so that intercomparisons and improvements to the aerosol classification schemes could be pursued in future works.

4.3 Interference filter

The choice for the interference filter was the *466-44 OD6 ULTRA Bandpass Filter* from Alluxa. Its transmission curve is depicted in Fig. 4.2. With a central wavelength of 466 nm and a full-width at half-maximum (FWHM) of 44 nm the interference filter's transmission band ranges from 444 to 488 nm, while an average transmission $> 92.5\%$ is provided in the 446 to 486 nm wavelength range. Outside of the filter band, a suppression of an optical depth of 6 (OD6) is provided in the wavelength ranges from 200 to 435 nm and 497 to 670 nm and of OD3 from 670 to 1100 nm. However, as the fluorescence backscatter signal is several orders of magnitude lower than the elastic returns (Veselovskii et al., 2020), a suppression higher than OD6 may be necessary for the elastic backscattering. To achieve an additional suppression, two interference filters were used in tandem, providing now OD12 suppression for the 355 and 532 nm laser wavelengths and OD6 suppression at 1064 nm.

4.4 Near-range channel

4.4.1 Setup

Due to delivery delays of the beam splitters for the fluorescence channel in the far-range receiver, the fluorescence channel was initially installed in the near-range receiver as a substitute. The new optical setup of the near-range detection unit is shown in Fig. 4.3.
To separate the UV branch (355 and 387 nm channels) from the fluorescence channel and the ones with longer wavelengths, a longpass dichroic beam splitter from Thorlabs with a cut-on wavelength of 425 nm was used. Its reflectance curve in Fig. 4.4 shows that more than 97% of the incoming radiation is reflected in a wavelength range from 330 to 410 nm. From 440 to 800 nm more than 95% are transmitted, which includes the transmission band of the fluorescence channel's interference filter, starting at 444 nm.
Subsequently, another beam splitter was required to reflect the spectral range of the fluorescence channel out of the beam and transmit the higher wavelengths for the other channels. For this purpose, a dichroic beam splitter with a cut-on wavelength of 505 nm

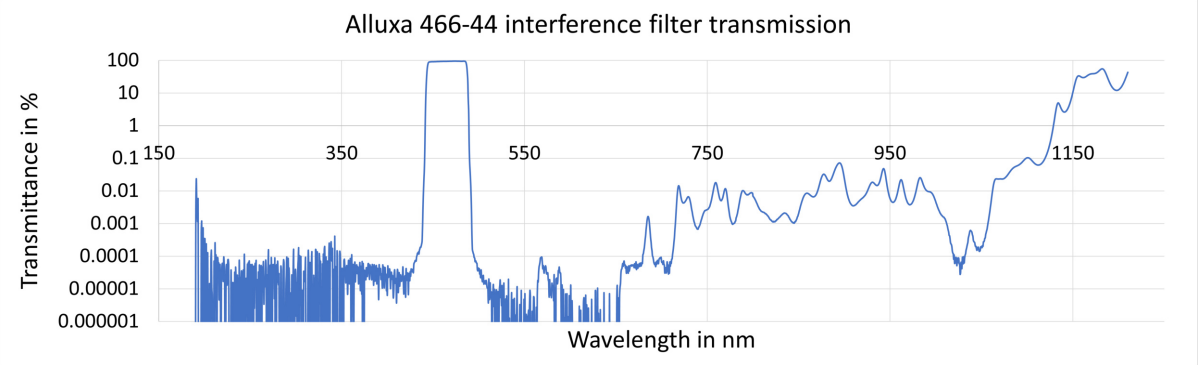

Figure 4.2: Transmission curve of the Alluxa 466 nm interference filter for the new fluorescence channel. Data were provided by Alluxa.

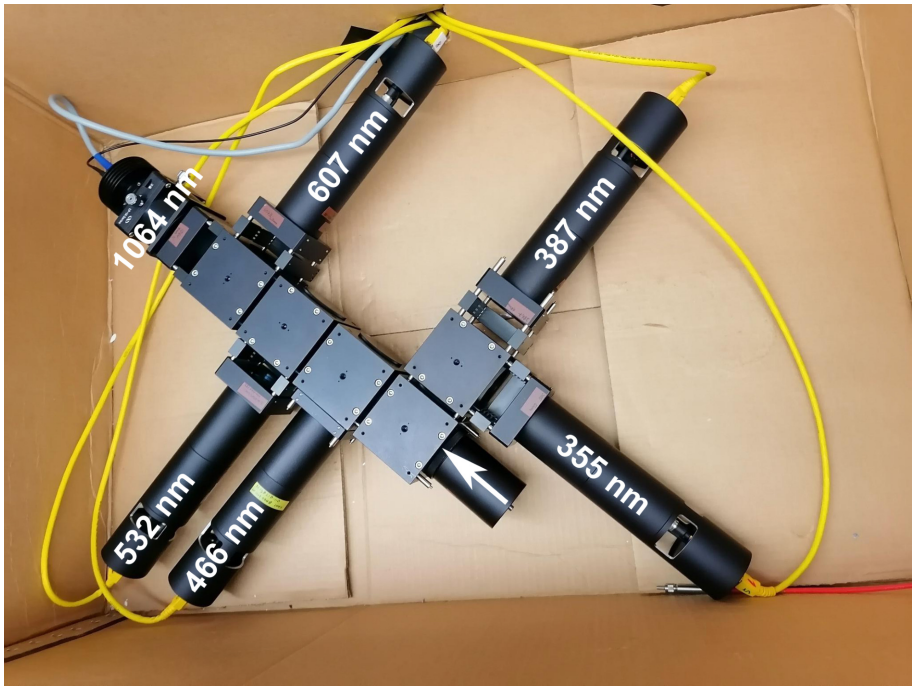

Figure 4.3: New setup of the near-range receiving unit of MARTHA.

was used. Fig. 4.5 shows > 97% reflectance from 380 to 490 nm and > 95% transmission from 525 to 830 nm. The distribution of the return signal into the remaining channels could still be realized with the beam splitters previously used for this purpose.
After the beam splitter, directly at the entrance of the detection tube, two one-inch interference filters are mounted, whose optical properties have already been described in Sec. 4.3. Behind the interference filters, two identical plano-convex N-BK7 lenses with a diameter of two inches and a focal length of 7.5 cm focus the beam onto the cathode. To reduce aberrations, the lenses are mounted with different orientation. The first lens is oriented with its planar side toward the incident radiation; the second one is mounted with its convex side toward the incident light.

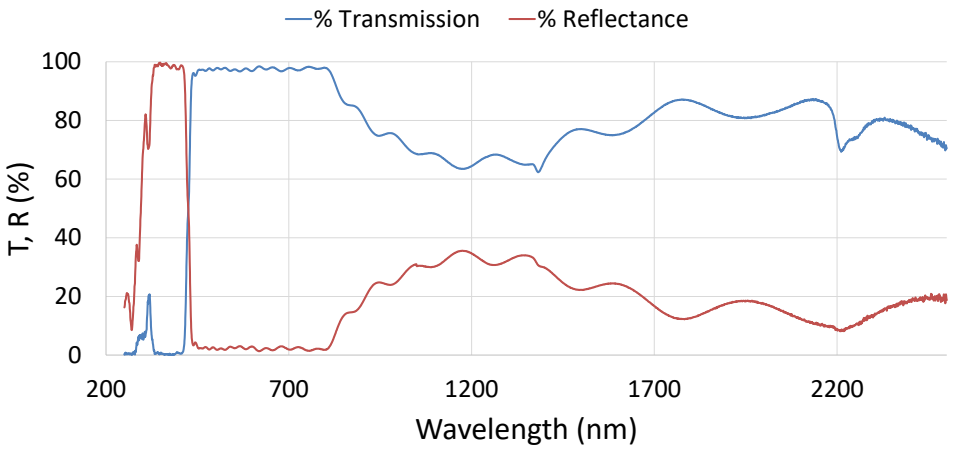

Figure 4.4: Reflection (red) and transmission (blue) curve of Thorlabs DMLP425L longpass dichroic beam splitter. Raw data were provided by Thorlabs.

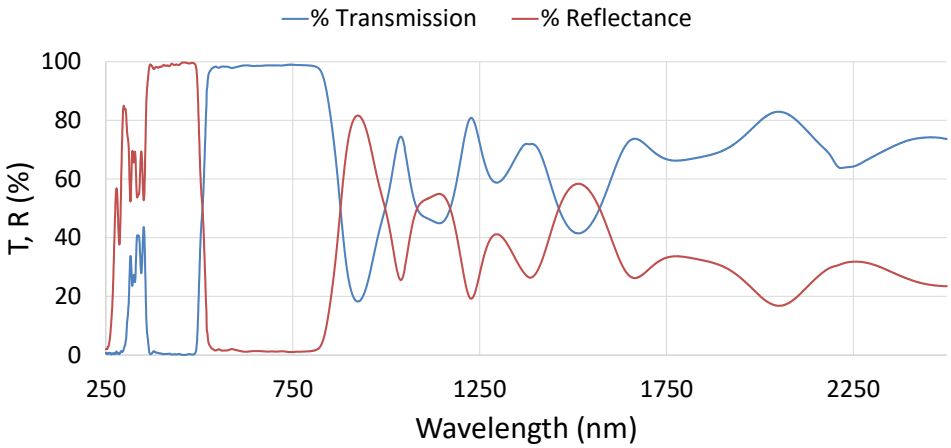

Figure 4.5: Reflection (red) and transmission (blue) curve of Thorlabs DMLP505L longpass dichroic beam splitter. Raw data were provided by Thorlabs.

4.4.2 Alignment of the near-range receiver

Before the new fluorescence channel could be used for measurements, the near-range receiver had to be readjusted. As the exchange or implementation of new beam splitters can change the beam path and add an additional beam shift, it had to be ensured that in all channels the light is imaged to the center of the detector. For this purpose, an alignment laser was coupled into the optical fiber inlet of the near-range receiver. The image of the laser beam, produced by each detection channel, was observed on a paper template, which had previously been placed just in front of the detector. A reticle on the template helped to align the laser spot to the center of the detector, which was accomplished by fine adjustments of the tilt angle of the respective beam splitters. Here, one always had to start with the foremost beam splitter in the beam path, since its alignment also influenced the beam path at all subsequent ones. Once all channels had been aligned correctly, the first measurements could be started.

4.4.3 Determination of the ratio of the optical system efficiencies η_R/η_F of the near-range receiver

At the beginning of a measurement on 16 June 2022, a calibration of the fluorescence backscatter coefficient was conducted. As it was already mentioned in Sec. 3, the ratio of the PMT detection efficiencies of the Raman and fluorescence channels has to be determined in order to obtain the ratio of the optical system efficiencies η_R/η_F for the calculation of β_F. Therefore, the detectors of the 387 nm Raman and the 466 nm fluorescence channels were exchanged and the ratio of the mean signals measured by both detectors was built for each channel. The calibration measurement showed that the PMT in the fluorescence channel had a higher detection efficiency than the one in the Raman channel. The value for the ratio of the detection efficiencies was about 0.893. The determination of η_R/η_F itself is described in the following.
Besides the detection efficiency of the PMT, the optical system efficiency of a lidar's de-

Table 4.1: Optical efficiencies of all transmitting or reflecting elements in the 387 nm and 466 nm NR channels.

NR channel	Nitrogen Raman (387 nm)	Fluorescence (466 nm)
First (common) beam splitter	$\mathcal{R}_1 = 98.9\%$	$\mathcal{T}_1 = 97\%$
Second (unique) beam splitter	$\mathcal{T}_2 = 90\%$	$\mathcal{R}_2 = 99.5\%$
Interference filters	$\mathcal{T}_3 = 60\%$	$\mathcal{T}_4 = 92.5\%$ ($\mathcal{T}_4{}^2$ because of 2 filters)
Neutral-density filters $\mathcal{T} = 10^{-\mathrm{OD}}$	OD = 1.5 $\mathcal{T}_{\mathrm{ND}} = 10^{-1.5} = 0.0316$	no neutral-density filters
Product $\prod_{i=1}^{N} \mathcal{T}_i \prod_{j=1}^{M} \mathcal{R}_j$	$\mathcal{R}_1\, \mathcal{T}_2\, \mathcal{T}_3\, \mathcal{T}_{\mathrm{ND}} = 0.0169$	$\mathcal{T}_1\, \mathcal{R}_2\, \mathcal{T}_4{}^2 = 0.8258$

tection channel includes also the optical efficiency of all elements along the light path in the detection unit (Wandinger, 2005a). I.e., the transmittances or reflectances of all optical elements (beam splitters, mirrors and interference filters) have to be considered, depending on whether a certain detector is positioned in transmission or reflection direction of the respective optical component. The overall system efficiency is then the product of these values:

$$\eta = \prod_{i=1}^{N} \mathcal{T}_i \prod_{j=1}^{M} \mathcal{R}_j\, \eta_{\mathrm{PMT}}, \tag{4.24}$$

with $\mathcal{T}_i$ the transmittance of the i-th optical component, $\mathcal{R}_j$ the reflectance of the j-th component, N the number of optical elements in transmission, M the number of elements in reflection and η_{PMT} the PMT detection efficiency.

For the near-range nitrogen Raman and fluorescence channels, these values are shown in Tab. 4.1. The two channels are separated at the first beam splitter, which reflects the 387 nm and transmits the 466 nm wavelength. As a result, the two wavelengths are now in different branches and are reflected (466 nm) or transmitted (387 nm) to their detector by two different beam splitters. As the fluorescence channel uses two identical interference filters in tandem, each interference filter contributes with the same transmission $\mathcal{T}_4 \times \mathcal{T}_4$. While no neutral-density (ND) filters are used in the fluorescence channel, the neutral-density filters in the nitrogen Raman channel, with a total optical density of 1.5, let only pass about 3.2% of the incident radiation. Hence, the optical efficiency of the 387 nm channel is significantly reduced to

$$\mathcal{R}_1\, \mathcal{T}_2\, \mathcal{T}_3\, \mathcal{T}_{\mathrm{ND}} = 0.989 \times 0.9 \times 0.6 \times 0.0316 = 0.0169. \tag{4.25}$$

In contrast, the efficiency of the fluorescence channel is substantially higher and amounts to

$$\mathcal{T}_1\, \mathcal{R}_2\, \mathcal{T}_4{}^2 = 0.97 \times 0.995 \times 0.925^2 = 0.8258. \tag{4.26}$$

Table 4.2: Detection efficiencies in the 466 nm NR fluorescence channel and overall system efficiency ratios for both the setup before and after the implementation of the far-range fluorescence channel.

	Original setup	After the implementation of the far-range fluorescence channel
Detection efficiency	$\eta^1_{\mathrm{det}} = 0.893$	$\eta^2_{\mathrm{det}} = 1.36$
Overall system efficiency ratio	$\frac{\eta_{\mathrm{R}}}{\eta^1_{\mathrm{F}}} = 0.0183$	$\frac{\eta_{\mathrm{R}}}{\eta^2_{\mathrm{F}}} = 0.0278$

For the detection efficiency, two cases must be distinguished. The detector originally used in the near-range channel (PMT_1, until 20 July 2022 in the near-range channel) has meanwhile been installed in the far-range channel (since 1 August 2022). Since both channels have been used together, another detector (PMT_2) has therefore been operated in the near-range channel (since September 2022). Its detection efficiency must of course be taken into account for the analysis of the more recent measurements. The detection efficiencies and resulting overall system efficiency ratios for both cases are shown in Tab. 4.2. As it was already stated above, the relative detection efficiency (ratio of the detection efficiencies of the 387 nm PMT and the 466 nm PMT) was

$$\eta^1_{\mathrm{det}} = \frac{\eta_{\mathrm{PMT,R}}}{\eta^1_{\mathrm{PMT,F}}} = 0.893 \tag{4.27}$$

for the original setup with PMT_1 in the near-range fluorescence channel. PMT_2 was much less sensitive. Hence, the relative detection efficiency for the setup after the implementation of the far-range fluorescence channel increased to

$$\eta^2_{\mathrm{det}} = \frac{\eta_{\mathrm{PMT,R}}}{\eta^2_{\mathrm{PMT,F}}} = 1.36. \tag{4.28}$$

Now, the ratios of the overall optical system efficiencies of the whole optical path of the channel can be calculated from these values for both cases by using Eq. (4.24):

$$\frac{\eta_{\mathrm{R}}}{\eta^1_{\mathrm{F}}} = \frac{\mathcal{R}_1\,\mathcal{T}_2\,\mathcal{T}_3\,\mathcal{T}_{\mathrm{ND}}}{\mathcal{T}_1\,\mathcal{R}_2\,{\mathcal{T}_4}^2}\,\eta^1_{\mathrm{det}} = 0.0183, \tag{4.29}$$

$$\frac{\eta_{\mathrm{R}}}{\eta^2_{\mathrm{F}}} = \frac{\mathcal{R}_1\,\mathcal{T}_2\,\mathcal{T}_3\,\mathcal{T}_{\mathrm{ND}}}{\mathcal{T}_1\,\mathcal{R}_2\,{\mathcal{T}_4}^2}\,\eta^2_{\mathrm{det}} = 0.0278. \tag{4.30}$$

In the data analysis, these ratios were finally used for the calculation of the fluorescence backscatter coefficient with Eq. (3.23). $\eta_{\mathrm{R}}/\eta^1_{\mathrm{F}}$ was used for the measurements until 20 July 2022, and from 1 August 2022 on $\eta_{\mathrm{R}}/\eta^2_{\mathrm{F}}$ was used.

4.5 Far-range channel

4.5.1 Setup

After the long-awaited beam splitters had finally been delivered, the fluorescence channel could be moved to the far-range receiver of the MARTHA system. The new optical setup of the far-range detection unit is sketched in Fig. 4.6.
The new fluorescence channel was placed in the branch with the lower wavelengths ahead of the 407 nm channel. Therefore, the first beam splitter along the optical path had to be replaced to ensure the transmission of the filter band of the fluorescence channel. A customized longpass dichroic beam splitter (BS1) from Laseroptik GmbH was chosen, a photograph of which is displayed in Fig. 4.7(a). Its transmission curve is shown in Fig. 4.8. While wavelengths > 520 nm are mainly transmitted, more than 99% of the incoming radiation is reflected at 355, 387, 407 nm and in the wavelength range from 440 to 490 nm, which includes the transmission band of the fluorescence channel's interference filter. In addition, a reflectivity of less than 1.5% at 607 nm, less than 0.8% at 1064 nm and less than 1% at 532 nm was guaranteed by the manufacturer.
Furthermore, another new beam splitter was required, which reflects the spectral range of the fluorescence channel out of the beam and transmits the lower wavelengths for the other UV channels. For this purpose, a short-pass beam splitter (BS2) was used, which is shown in Fig. 4.7(b). Its transmission curve in Fig. 4.9 shows more than 98% reflectance (on average even more than 99.7%) from 440 to 490 nm and less than 1% reflectance at 355 nm, less than 2% at 387 nm and less than 4% at 407 nm. The other beam splitters could still be used as they were before.

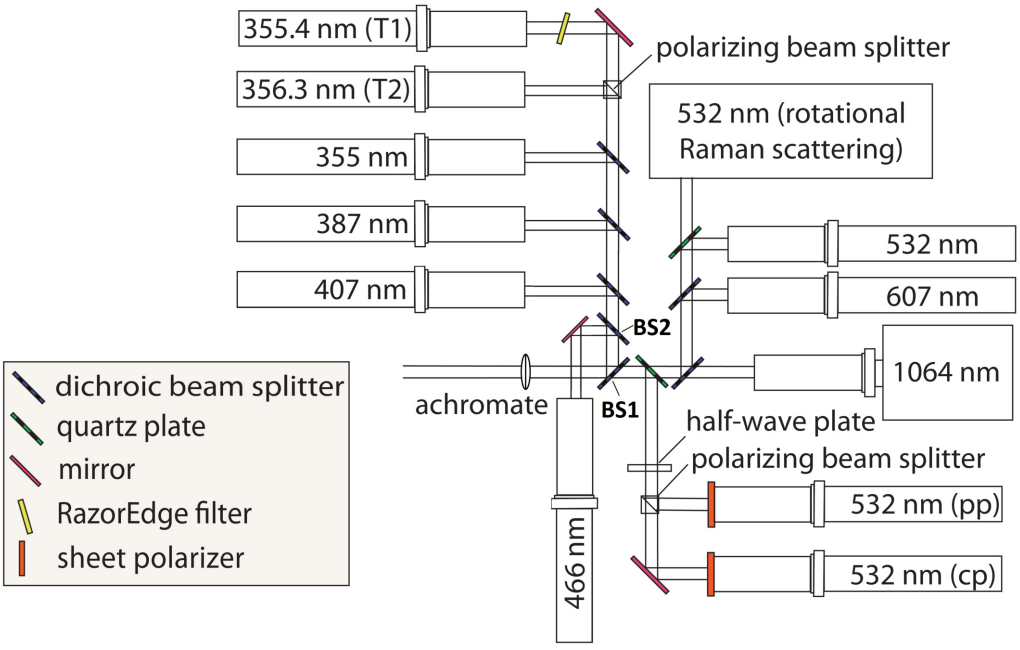

Figure 4.6: New setup of the MARTHA far-range receiver after the implementation of the fluorescence channel at 466 nm.

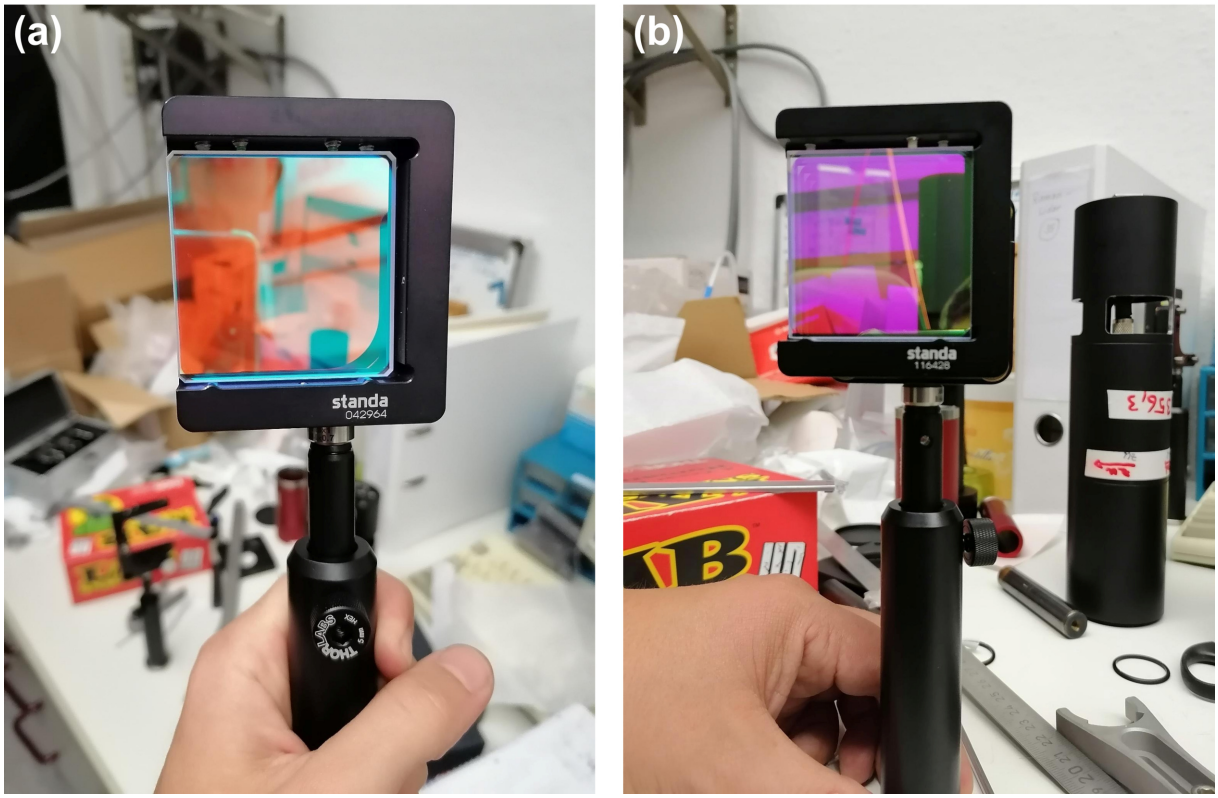

Figure 4.7: (a) Photograph of the first beam splitter (BS1) with high reflectance (HR) at 355, 387, 407, 440−490 nm and high transmission (HT) at 532−560, 607, 1064 nm. (b) Photograph of the second beam splitter (BS2) with HT at 355, 387, 407 nm and HR at 440−490 nm.

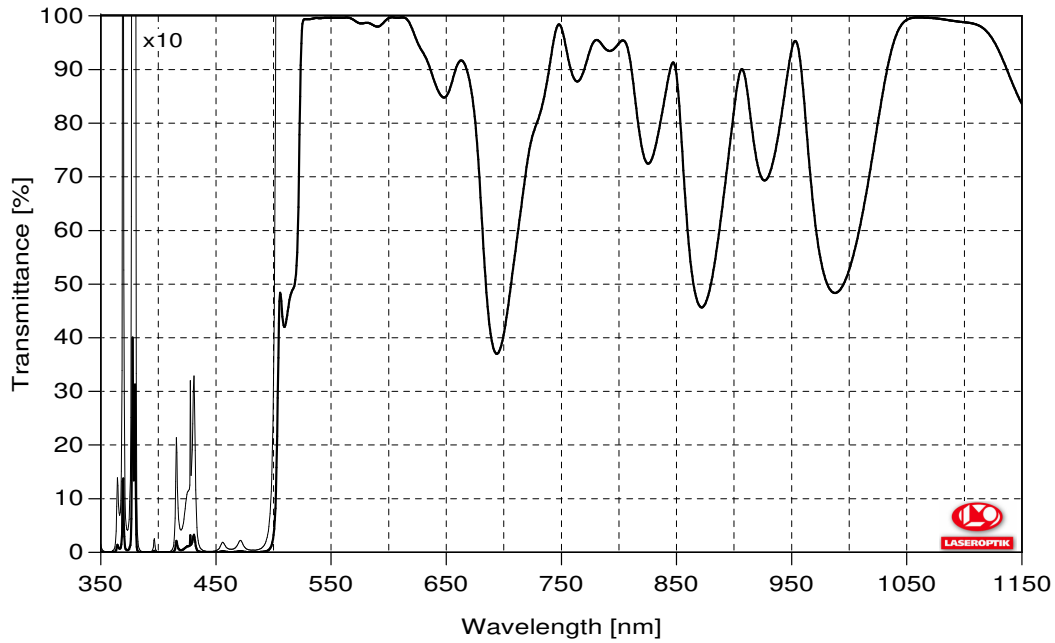

Figure 4.8: Transmission curve of the first beam splitter (BS1) with HR at 355, 387, 407, 440−490 nm and HT at 532−560, 607, 1064 nm.

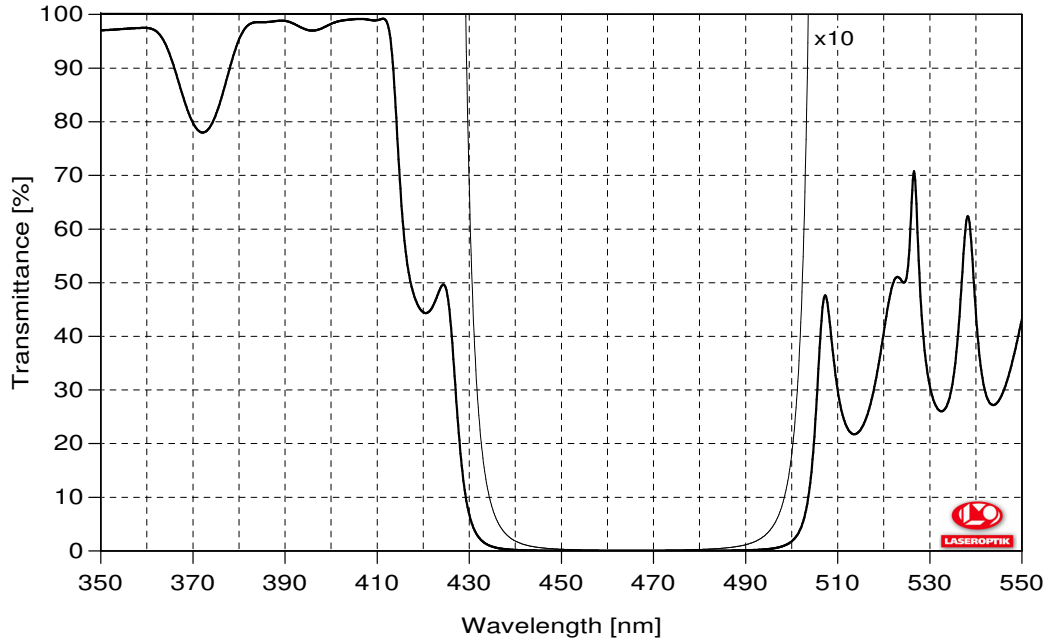

Figure 4.9: Transmission curve of the second beam splitter (BS2) with HT at 355, 387, 407 nm and HR at 440−490 nm.

The setup of the new far-range fluorescence channel itself is sketched in Fig. 4.10. Since there was not enough space for another detection tube in a straight line behind the second beam splitter, a dielectric mirror was used to redirect the beam towards a still empty space in the receiving unit. As a result, the light that is reflected into the fluorescence channel first crosses the incoming beam from the telescope, before it reaches the detection tube. There, as the first component after the beam splitter, a lens system consisting of two plano-convex N-BK7 lenses with a diameter of two inches serves as the objective. To reduce aberrations, the lenses are mounted in different orientation. The first lens (L1 in Fig. 4.10) has a focal length of 1 m and is oriented with its planar side toward the incident radiation. The second one (L2) is mounted with its convex side toward the incident light and has a smaller focal length of 30 cm. Behind the lenses, two one-inch interference filters are mounted, whose optical properties have already been described in Sec. 4.3.
Finally, in front of the detector, a lens system consisting of two identical one-inch lenses (L3) serves as an ocular, which images the primary mirror of the telescope onto the photocathode of the PMT. Again, the plano-convex lenses are made of N-BK7 as a substrate with a focal length of 12.5 cm and are mounted with different orientation.
All four lenses that are used in this setup are equipped with an anti-reflection coating for the 400 to 1000 nm spectral range. The anti-reflection coating minimizes the amount of light that is reflected at the various lens surfaces. Thus, multiple reflections are prevented, and the transmission is increased, which is crucial for this application as the fluorescence backscatter signal is very low.

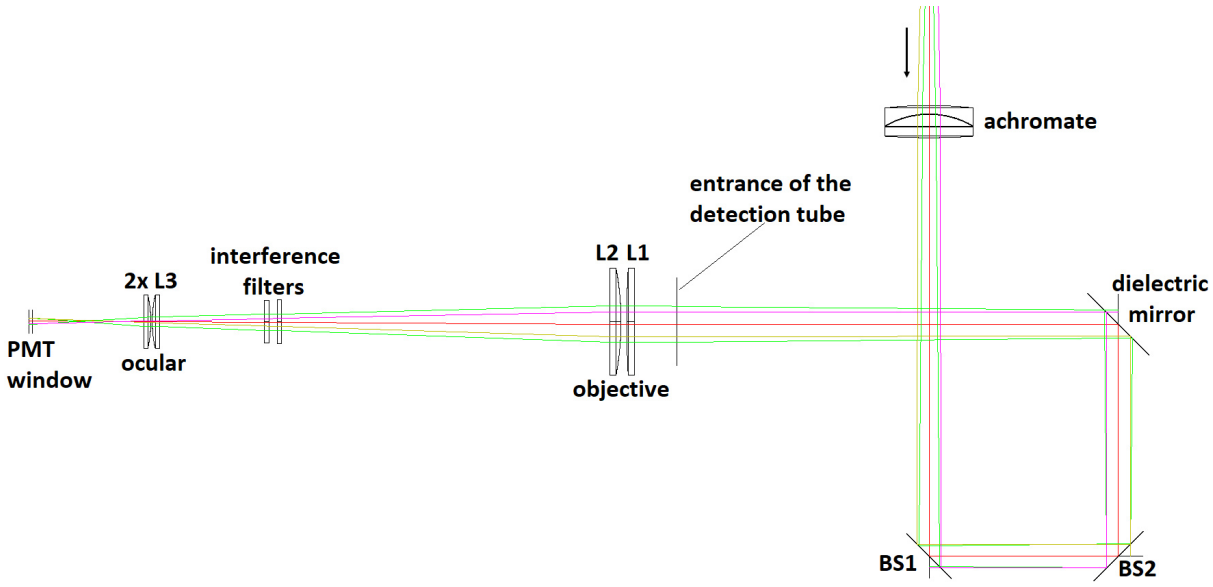

Figure 4.10: Optical setup of the new far-range fluorescence channel in MARTHA. The ray path was calculated with ZEMAX.

4.5.2 Alignment of the far-range receiver

The far-range receiver had to be realigned after the beam splitters had been replaced or newly installed. For this purpose, an alignment laser was placed at the entrance of the far-range receiver in order to visualize the path of the backscattered light collected by the telescope. To ensure that the light is imaged to the center of the detector in all channels, a template made of graph paper was put on the entrance of each detection tube one after the other. This principle is shown on the photograph in Fig. 4.11(a). As it can be seen, multiple light points were imaged onto the template by multiple reflections from the optical components. Once the main reflection was found by gradually shading the reflections, it had to be moved to the center of the reticle by fine adjustments of the tilt angle of the respective beam splitters. For the new fluorescence channel, the correct alignment was additionally checked directly in front of the detector. For this purpose, the template was placed on the end of the detection tube instead of the detector, as shown in Fig. 4.11(b). Once all channels had been aligned correctly, the new far-range fluorescence channel was ready to measure.

4.5.3 Determination of the ratio of the optical system efficiencies η_R/η_F of the far-range receiver

The ratio of the optical system efficiencies was determined in the same way as for the near-range Raman and fluorescence channels in Sec. 4.4.3. During one of the first measurements with the new far-range fluorescence channel, its detector was swapped with the one of the 387 nm far-range channel and the mean signal ratio measured by both detectors was calculated for each channel.

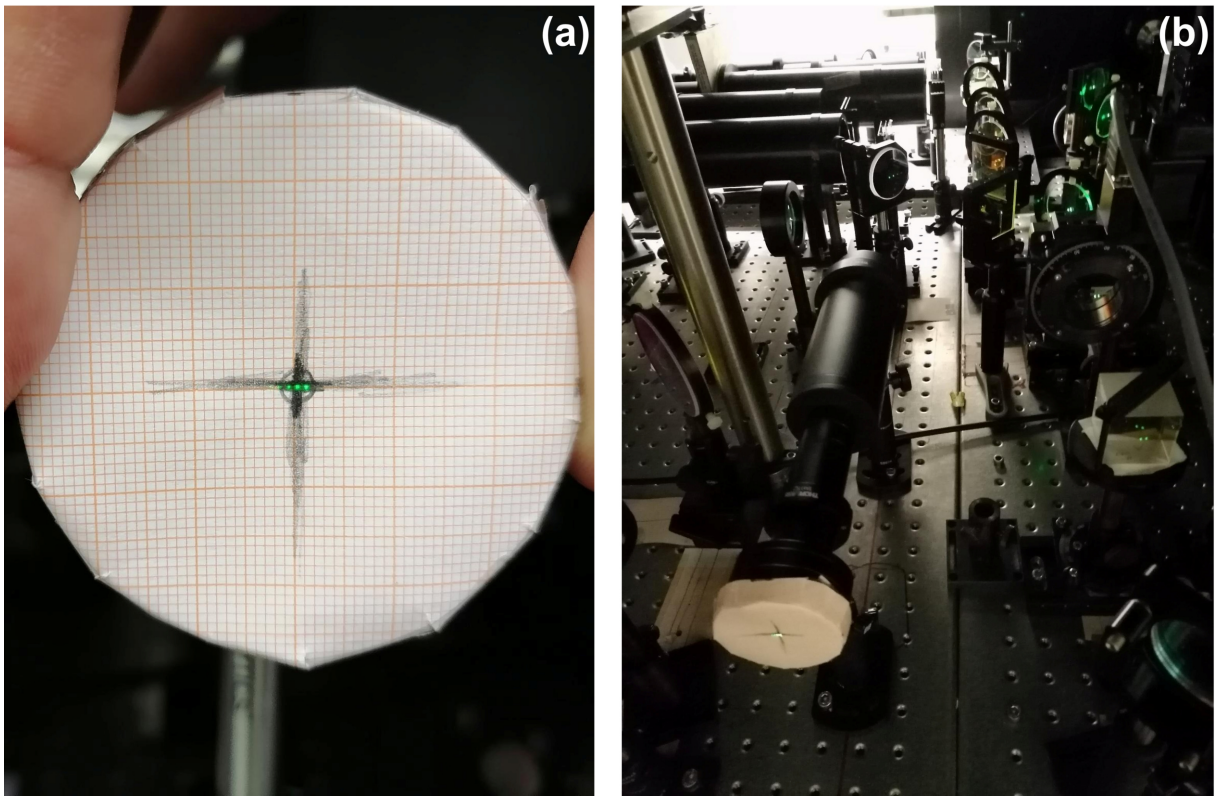

Figure 4.11: (a) Photograph of the alignment of the far-range receiver. A template made of graph paper with a reticle on it is placed on the entrance of the detection tubes. (b) Photograph of the additional alignment of the far-range fluorescence channel. Here, the template was also placed on the end of the detection tube instead of the detector.

In this case, the PMT in the 466 nm fluorescence channel had a lower detection efficiency than the one in the 387 nm Raman channel. The value for the ratio of the detection efficiencies was

$$\eta^3_{\mathrm{det}} = \frac{\eta_{\mathrm{PMT,R}}}{\eta^3_{\mathrm{PMT,F}}} = 1.4155. \tag{4.31}$$

The optical efficiencies of all transmitting or reflecting elements in the nitrogen Raman and fluorescence far-range channels were again calculated by their transmittances or reflectances, which are shown in Tab. 4.3. The beam splitter BS1 does not have to be considered for the calculation because both channels are located in its reflection branch. The two channels are separated at the newly installed beam splitter BS2, which reflects the 466 nm and transmits the 387 nm wavelength. As a result, the two wavelengths are now in different branches and move on through different further optical components. The 387 nm radiation is first transmitted by a beam splitter selecting the water-vapor channel at 407 nm and then reflected by another beam splitter to its detection tube. In contrast, the wavelength range around 466 nm is only deflected by a dielectric mirror with very high reflectivity towards the detection tube of the fluorescence channel (see Fig. 4.6).
As the fluorescence channel uses two identical interference filters in tandem, its transmit-

Table 4.3: Transmittances or reflectances of all optical elements in the 387 nm and 466 nm FR channels.

FR channel	Nitrogen Raman (387 nm)	Fluorescence (466 nm)
Common beam splitter (BS2)	$\mathcal{T}_5 = 97.1\%$	$\mathcal{R}_3 = 98\%$
Further (unique) optical elements	beam splitter 407 nm: $\mathcal{T}_6 = 94.5\%$ beam splitter 387 nm: $\mathcal{R}_4 = 95\%$	dielectric mirror $\mathcal{R}_5 = 99.75\%$
Interference filters	$\mathcal{T}_7 = 70\%$	$\mathcal{T}_4 = 92.5\%$ ($\mathcal{T}_4{}^2$ because of 2 filters)
Neutral-density filters $\mathcal{T} = 10^{-\mathrm{OD}}$	OD = 1.5 $\mathcal{T}_{\mathrm{ND}} = 10^{-1.5} = 0.0316$	no neutral-density filters
Product $\prod_{i=1}^{N} \mathcal{T}_i \prod_{j=1}^{M} \mathcal{R}_j$	$\mathcal{R}_4\ \mathcal{T}_5\ \mathcal{T}_6\ \mathcal{T}_7\ \mathcal{T}_{\mathrm{ND}} = 0.0193$	$\mathcal{R}_3\ \mathcal{R}_5\ \mathcal{T}_4{}^2 = 0.8364$

tance $\mathcal{T}_4$ must be squared. While no neutral-density filters are used in the fluorescence channel, the neutral-density filters in the nitrogen Raman channel, with a total optical density of 1.5, let only pass about 3.2% of the incident radiation. This significantly reduces the optical efficiency of the 387 nm channel to

$$\mathcal{R}_4\ \mathcal{T}_5\ \mathcal{T}_6\ \mathcal{T}_7\ \mathcal{T}_{\mathrm{ND}} = 0.971 \times 0.945 \times 0.95 \times 0.7 \times 0.0316 = 0.0193. \tag{4.32}$$

In contrast, the efficiency of the fluorescence channel is substantially higher and amounts to

$$\mathcal{R}_3\ \mathcal{R}_5\ \mathcal{T}_4{}^2 = 0.98 \times 0.9975 \times 0.925^2 = 0.8364. \tag{4.33}$$

Now the ratio of the overall optical system efficiencies can be calculated by using Eq. (4.24):

$$\frac{\eta_{\mathrm{R}}}{\eta_{\mathrm{F}}^3} = \frac{\mathcal{R}_4\ \mathcal{T}_5\ \mathcal{T}_6\ \mathcal{T}_7\ \mathcal{T}_{\mathrm{ND}}}{\mathcal{R}_3\ \mathcal{R}_5\ \mathcal{T}_4{}^2}\ \eta_{\mathrm{det}}^3 = 0.0327. \tag{4.34}$$

5 Results and discussion

In this chapter, three measurement cases are presented in order to demonstrate the performance of the newly implemented fluorescence channels for the detection and typing of atmospheric aerosol layers. In a second step, a first statistical analysis regarding the measured fluorescence quantities is presented and the results are briefly compared to previous findings in the literature.

5.1 Measurement strategy

The atmospheric aerosol fluorescence measurements used in this thesis were carried out from June to October 2022. As Veselovskii et al. (2020) showed, the fluorescence signal is very weak, i.e., the fluorescence backscatter coefficient is several orders of magnitude lower than corresponding elastic backscatter coefficients. Therefore, the measurements could only be performed during night time, since the fluorescence signal is embedded in the solar spectrum and measured with a quite broad filter width (at $466 \pm 22\,\mathrm{nm}$). Consequently, during the day the scattered solar radiation passing the filter is higher than the actual fluorescence signal, so that the signal in the fluorescence channel completely consists of noise.
Furthermore, MARTHA is a manually operated lidar system, which makes regular measurements challenging. Thus, after some test measurements, the focus was initially on nights when increased concentrations of fluorescent aerosol could be expected, such as the smoke event on 18 and 19 July 2022, when large amounts of wildfire aerosol and Saharan dust dimmed the atmosphere over Leipzig. Later on, a series of measurements was conducted on several consecutive nights between 10 and 21 October 2022 to get an idea of the typical magnitude of the fluorescence signal during normal, unpolluted nights.
Due to continuous improvements of the fluorescence channels, the setup changed during the measurement period (see Chapter 4). In the beginning of summer, only one pair of fluorescence filters was available. This filter set was first integrated into the near-range receiver. At the end of July, the pair of filters was implemented in the far-range receiver. In September 2022, a second set of fluorescence filters was available, so that now both the near-range and the far-range receiver could be equipped with fluorescence channels.

5.2 A thin smoke layer beneath cirrus – case of 16 June 2022

The first measurement example presented here is from the night of 16–17 June 2022. The height-time distribution of the range-corrected lidar signal at 1064 nm for the measurement time from 21:15−01:15 UTC is depicted in Fig. 5.1(a). It showed a quite polluted boundary layer, where the strongest signal was found at its top at around 2 km height. In the free troposphere, cirrus clouds were located above 6 km height with a vertical extent up to 9 km height. Below the cirrus, a thin aerosol layer ranged from 5−6 km. The height of this layer was decreasing with time.

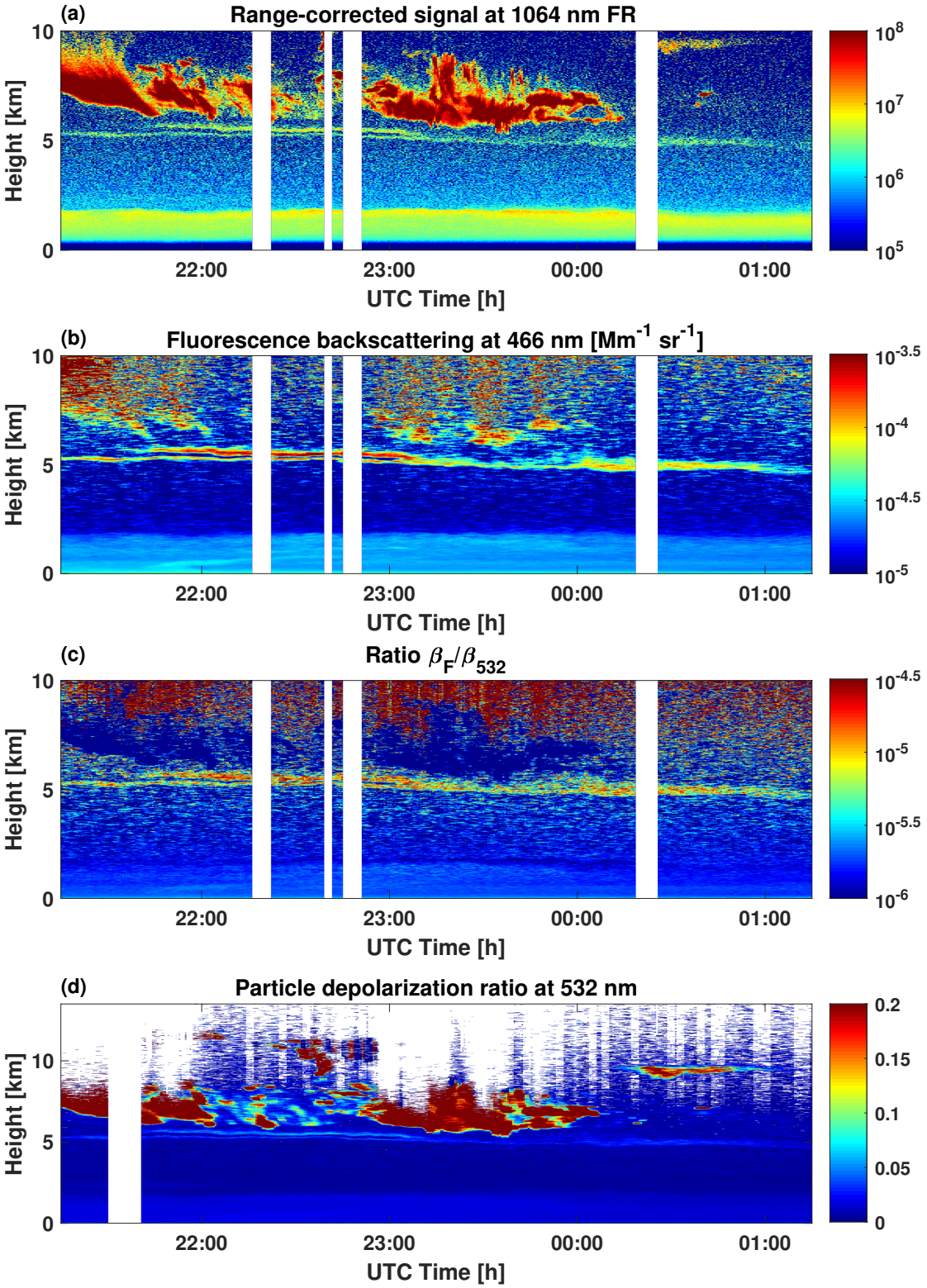

Figure 5.1: Height-time distributions of the (a) range-corrected lidar signal at 1064 nm, (b) fluorescence backscatter coefficient at 466 nm, (c) fluorescence capacity (ratio of fluorescence backscatter coefficient to 532 nm particle backscatter coefficient) measured with MARTHA and (d) particle depolarization ratio at 532 nm measured with Polly^{XT} at Leipzig on 16−17 June 2022.

Fig. 5.1(b) shows the height-time distribution of the 466 nm fluorescence backscatter coefficient. The boundary layer was only weakly fluorescing with a β_{Fluo} of around $2.6 \times 10^{-5}\,\mathrm{Mm^{-1}\,sr^{-1}}$. Above it, the fluorescence backscatter coefficient reduced to values of $0.8{-}1 \times 10^{-5}\,\mathrm{Mm^{-1}\,sr^{-1}}$, what can be regarded as a background value because the height range of 2−5 km was quite particle-free as the low 1064 nm signal in Fig. 5.1(a) demonstrates. The clouds also evoked a fluorescence signal, although this did not affect the whole area of the clouds, but only individual speckles. There, β_{Fluo} reached $2 \times 10^{-5}\,\mathrm{Mm^{-1}\,sr^{-1}}$ in the temporal mean. However, since ice does not fluoresce, these are probably cross-talk effects with the 355 and 532 nm elastic channels. I.e., due to an insufficient efficiency of the wavelength separation by the beam splitters used in the near-range receiver, a considerable part of the strong elastically backscattered radiation by the cloud reaches the fluorescence channel, so that the suppression of elastic scattering by the interference filters is too low and some photons at 355 and 532 nm pass through the fluorescence filters. To distinguish this type of fluorescence signal from the actual fluorescent aerosol, the fluorescence backscatter coefficient is normalized by the 532 nm particle backscatter coefficient:

$$G_{\mathrm{F}} = \frac{\beta_{\mathrm{Fluo}}}{\beta_{532}^{\mathrm{par}}}. \tag{5.35}$$

This quantity is the so-called fluorescence capacity G_{F}. For a first visual impression, Fig. 5.1(c) shows the height-time distribution of the ratio of β_{Fluo} to the 532 nm aerosol backscatter coefficient calculated using a simplified approach, as the Raman retrieval was only applied for the calculation of time-averaged vertical profiles of the backscatter coefficients. This ratio is already similar to G_{F}, which uses the $\beta_{532}^{\mathrm{par}}$ calculated by the Raman retrieval (cf. Fig. 5.2(a)). Fig. 5.1(c) reveals the clouds by a minimum in this backscatter ratio (blue colors), while the aerosol layer shows high values (orange to red colors). So, G_{F} is a useful parameter to easily distinguish clouds and fluorescent aerosol layers by visual means.

Now, the most interesting feature of this measurement shall be investigated – the aerosol layer at 5−6 km height. To get a more accurate picture, the total measurement time was divided into two periods of two hours each. In the first period from 21:15−23:15 UTC, the fluorescent layer was higher (5.5 km) than in the second period from 23:15−01:15 UTC (5 km). As an example, the first period is examined here in more detail.

The time-averaged vertical profiles of the 532 nm elastic and fluorescence backscatter coefficients together with the fluorescence capacity for the time period from 21:15−23:15 UTC are shown in Fig. 5.2(a). The mean fluorescence backscatter coefficient reached a maximum of $8.6 \times 10^{-5}\,\mathrm{Mm^{-1}\,sr^{-1}}$ at 5.5 km height. With a corresponding 532 nm particle backscatter coefficient of $0.635\,\mathrm{Mm^{-1}\,sr^{-1}}$, G_{F} amounted to 1.4×10^{-4}. These backscatter profiles in Fig. 5.2(a) also corroborate again the usefulness of the fluorescence capacity as an analysis quantity. While β_{Fluo} was enhanced (up to $4.2 \times 10^{-5}\,\mathrm{Mm^{-1}\,sr^{-1}}$) in the height range of the cloud, the higher β_{532} values of more than $10\,\mathrm{Mm^{-1}\,sr^{-1}}$ led to a very low G_{F} of about $1{-}3 \times 10^{-6}$ in the cloud.

In a next step, the aerosol type of the fluorescing layer shall be determined. Besides the

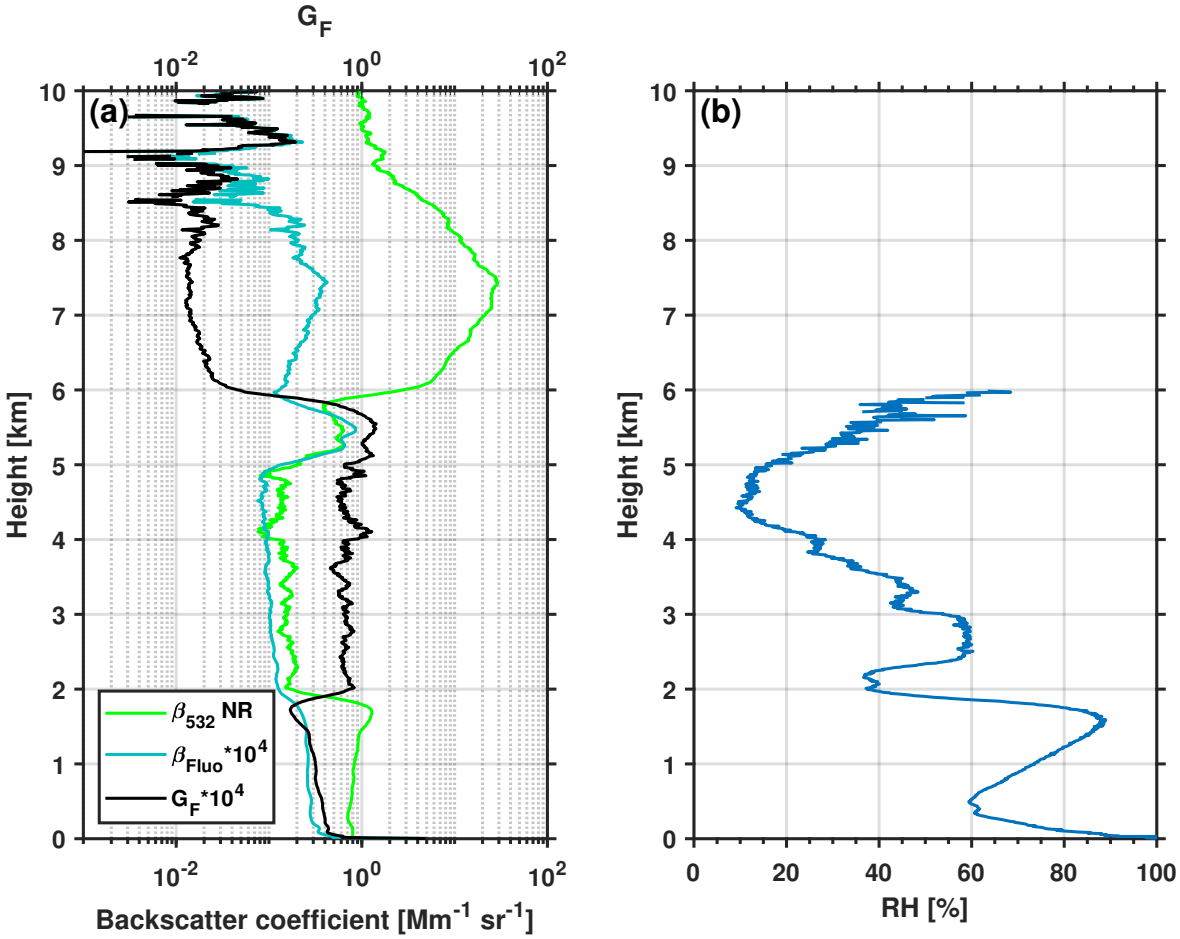

Figure 5.2: Vertical profiles of (a) aerosol ($\beta_{532}^{\mathrm{NR}}$) and fluorescence backscatter coefficients (β_{Fluo}) together with the fluorescence capacity (G_{F}) and (b) relative humidity (RH) averaged over the time period from 21:15−23:15 UTC on 16 June 2022.

fluorescence capacity the particle depolarization ratio is used to characterize the aerosol. Unfortunately, the MARTHA polarization channels were out of order during the last months. For this reason, we used the depolarization ratio at 532 nm from Polly$^{\mathrm{XT}}$ measurements. The Polly$^{\mathrm{XT}}$ system measured continuously at TROPOS during 2022, so that during all MARTHA measurements, measurements of Polly$^{\mathrm{XT}}$ are also available. The particle depolarization ratio at high temporal resolution is presented in Fig. 5.1(d). While the cirrus shows a high depolarization ratio of $> 20\,\%$, the fluorescing aerosol layer under investigation shows a particle depolarization ratio of around 5−7 %, which is enhanced compared to the background, but still quite low. Such moderate depolarization values are typical for wildfire smoke particles that were rapidly lofted into a dry air mass, so that aging and the development of a spherical core-shell structure of the particles is mostly prevented (Engelmann et al., 2021; Ohneiser et al., 2022).

Another indicator of aerosol type is the lidar ratio. To determine the lidar ratio, the vertical mean of the time-averaged extinction and backscatter coefficients was calculated over the height range from 50 height bins (= 375 m) below to 50 bins above the center

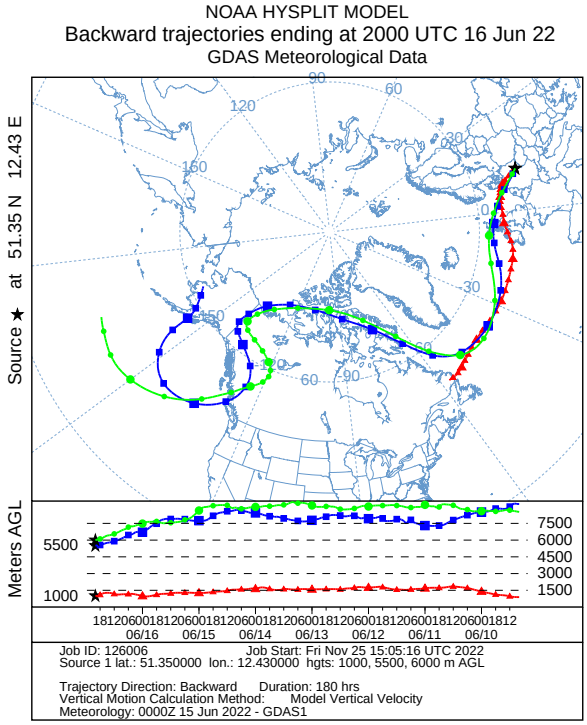

Figure 5.3: HYSPLIT backward trajectories for the arrival heights 1, 5.5 and 6 km at Leipzig at 20 UTC on 16 June 2022.

of the aerosol layer. From these values, the lidar ratios were calculated with Eq. (2.12), although there are quite large uncertainties as the layer is quite thin. For the considered aerosol layer, the 532 nm lidar ratio ($S_{532} = 61 \pm 10$ sr) was significantly higher than the one at 355 nm ($S_{355} = 41 \pm 10$ sr). This unusual wavelength dependence of the lidar ratio is an unambiguous sign of smoke, where the difference is typically > 20 sr (Ohneiser et al., 2021). Thus, in combination with the other properties (enhanced fluorescence capacity and enhanced depolarization ratio), it can be concluded that the considered aerosol layer consisted of wildfire smoke.

The observed smoke layer was very dry. The time-averaged relative humidity (RH) measured with MARTHA is displayed in Fig. 5.2(b). In the considered smoke layer the RH was 15−45 %. This finding corroborates the hypothesis that particle aging was not finalized and the smoke particles were still nonspherical so that the particle depolarization ratio was enhanced.

To identify the smoke source region, backward trajectories were computed with the HYSPLIT model. Backward trajectories arriving over Leipzig on 16 June 2022, at 20 UTC, are shown in Fig. 5.3. The model was run for arrival heights of 1, 5.5 and 6 km and a duration of 180 h. The trajectories show that the planetary boundary layer was influenced by air masses crossing Ireland, Scotland, and the northwest of Germany. The air mass, in which the observed smoke layer was embedded (5 to 6 km height), originated from the most northern parts of the American continent. Around the 10 June 2022, the 5500 m trajectory started in the southwest of Alaska, where strong wildfires were burning at that

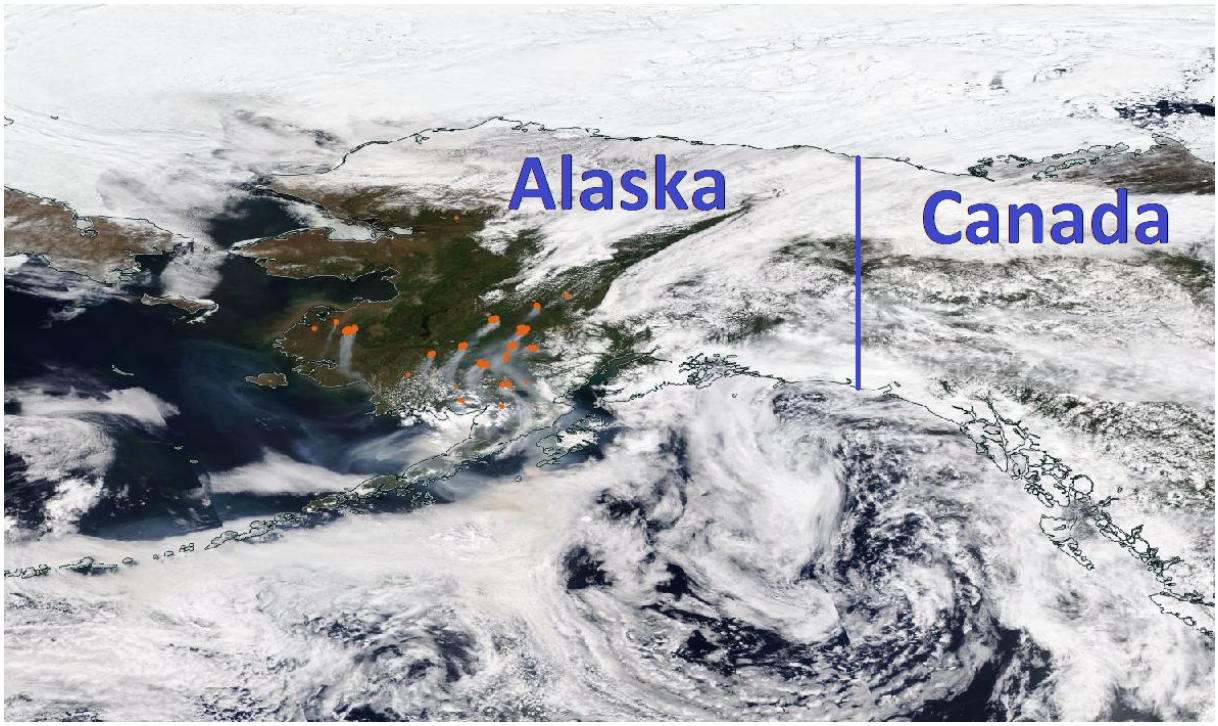

Figure 5.4: NASA Worldview scene *Satellite Detections of Fire* for Alaska on 10 June 2022. Red dots indicate fire spots (source: https://worldview.earthdata.nasa.gov; last access on 4 July 2022).

time. A satellite image of this day from NASA WorldView in Fig. 5.4 shows several large wildfire spots in the Lake Clark National Park north of the Alaska Peninsula and a bit further north in the Denali National Park in the Alaska Range. As the simulated backward trajectory in Fig. 5.3 passes over this area, it can be concluded that these Alaska wildfires were probably the source region of the wildfire smoke observed at Leipzig on 16 June 2022. The great heights of the trajectory over the regions of the wildfires support the hypothesis of a fast lofting of the smoke particles into the dry upper troposphere by pyrocumulonimbus convection.

5.3 Complex dust-smoke mixture over Leipzig – case of 19 July 2022

In the middle of July 2022, a number of severe wildfires occurred in southern France and the Iberian Peninsula, e.g., in Galicia in the northwest of Spain and the Sierra de Gata in the west of Spain at the border to Portugal, as shown by the satellite fire detection product in Fig. 5.5. Large amounts of biomass-burning aerosol were released into the atmosphere and subsequently transported to Germany by favorable air flow conditions. Since 18 July 2022, Germany was increasingly influenced by a high-pressure ridge that was approaching from the southwest. Fig. 5.6 illustrates the synoptic situation at 18 UTC on 19 July, showing the surface pressure, the geopotential height at 500 hPa and

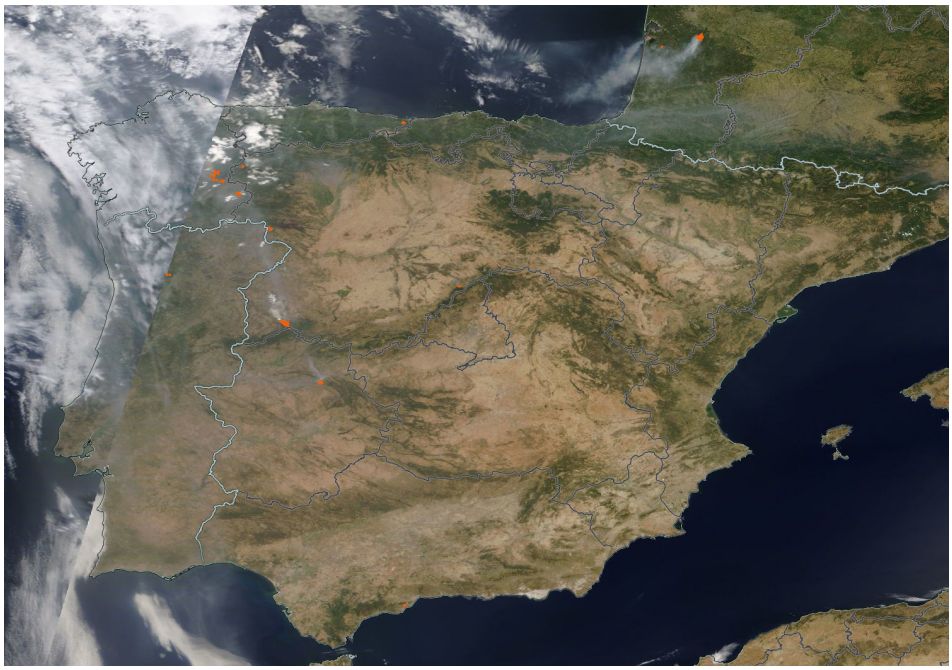

Figure 5.5: NASA Worldview scene *Satellite Detections of Fire* for the Iberian Peninsula on 15 July 2022. Red dots indicate fire spots (source: https://worldview.earthdata.nasa.gov; last access on 28 November 2022).

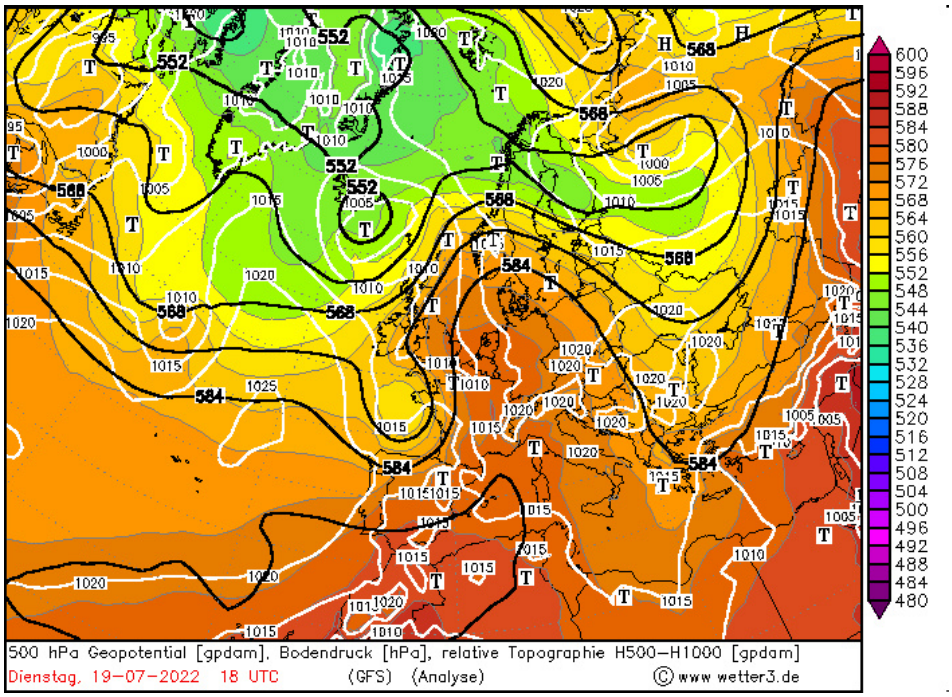

Figure 5.6: Synoptic situation over Europe on 19 July 2022 at 18 UTC: surface pressure (white isolines), 500 hPa geopotential height (black isolines) and relative topography (colored contours). (Source: https://wetter3.de; Last access on 28 November 2022).

the relative topography. Leipzig, which had been on the front side of the ridge the day before, was now below the ridge axis, causing the high-altitude winds to approach from southerly to southwesterly directions. As a result, air masses from the Iberian Peninsula were advected on the back side of the ridge, containing large amounts of wildfire smoke. The high aerosol load resulted in a dimmed sky over Leipzig. We used this unique opportunity for intensive lidar measurements. Figs. 5.7(a) and 5.7(b) show the height-time distributions of the range-corrected lidar signal at 1064 nm and the fluorescence backscatter coefficient, respectively. The data are displayed for the whole measurement period from 19 July 2022, 20:30 UTC, to 20 July 2022, 02:15 UTC. They reveal a very polluted troposphere, which contained several aerosol layers reaching up to 6.5 km height. The boundary layer extended up to 2 km altitude, showing a strong 1064 nm signal and a moderate fluorescence backscatter coefficient ($\beta_{\mathrm{Fluo}} \approx 4 \times 10^{-5}\,\mathrm{Mm^{-1}\,sr^{-1}}$). Trajectories suggest that this air mass started from the Iberian Peninsula around a week before. Thus, in addition to traffic exhaust and urban air pollution, it probably also contained aged smoke particles from western Spain and Portugal, which caused the observed moderate fluorescence in this layer. Above the boundary layer, several aerosol layers can be seen up to 6.5 km altitude. The optically thickest layers (causing the strongest signals at 1064 nm) are found between 4.5 and 5 km at the beginning of the measurement (further referred to as layer 1) and around 2.5−3.5 km at the end of the measurement (layer 2). These two layers are analyzed in Sec. 5.3.1. Another strongly fluorescent layer (layer 3) formed at 5.5 km altitude, as discussed in Sec. 5.3.2. Finally, Sec. 5.3.3 examines a fluorescent layer occurring in the boundary layer at around 1.25 km height at the end of the measurement.

5.3.1 Dust-smoke mixtures (layers 1 and 2)

Layer 1 showed the strongest fluorescence backscatter coefficient of $1.45 \times 10^{-4}\,\mathrm{Mm^{-1}\,sr^{-1}}$ at 4.6 km height. Layer 2 was only moderately fluorescent ($\beta_{\mathrm{Fluo}} \approx 6.7 \times 10^{-5}\,\mathrm{Mm^{-1}\,sr^{-1}}$). The particle depolarization ratio, which is shown in Fig. 5.7(c), reveals a possible reason for that. In layer 2 at 2.5−3.5 km height, the particle depolarization ratio at 532 nm was enhanced with values of up to 7.5 % at the layer top, while it was much lower ($\delta_{\mathrm{par}} \approx 3\,\%$) in the higher layer 1. This finding indicates the presence of dust particles in the lower layer 2, which explains the lower β_{Fluo} despite the high β_{1064}. I.e., layer 2 seems to be a dust-smoke mixture, while layer 1 appears to be more dominated by pure smoke.
This assumption is supported by simulations of the air-mass-source tool of Radenz et al. (2021). This tool combines particle positions from a dispersion model with land cover information by summing up all time periods during which the corresponding air mass was below a so-called reception height above a certain terrain. The sum represents the so-called residence time over the relevant terrain. Fig. 5.8 shows the vertical profiles of the normalized residence time of the air mass that was over Leipzig during the considered lidar observation, considering a reception height of 5 km. According to the model calculations, the air mass at 3.5−4 km height spent about 15 % of its time below 5 km over the Sahara

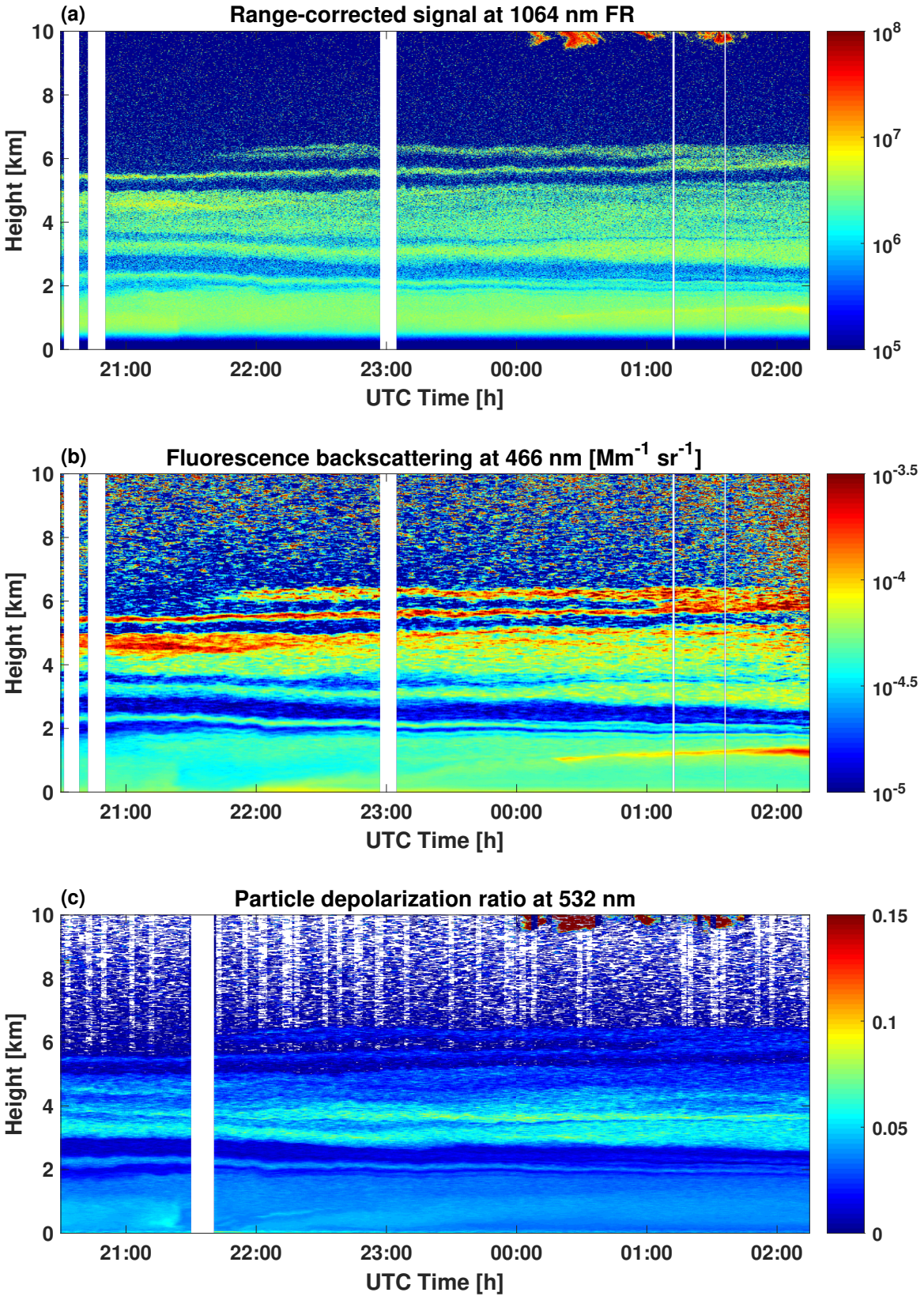

Figure 5.7: Height-time distributions of the (a) range-corrected lidar signal at 1064 nm, (b) fluorescence backscatter coefficient at 466 nm measured with MARTHA and (c) particle depolarization ratio at 532 nm measured with Polly^{XT} at Leipzig on 19−20 July 2022.

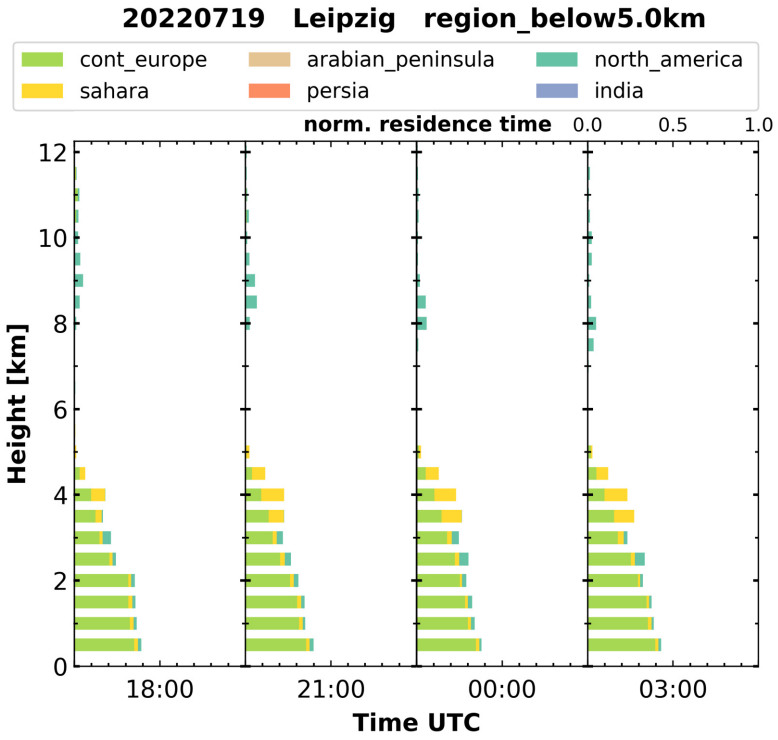

Figure 5.8: Air-mass-source estimate from 18 UTC on 19 July 2022 to 3 UTC on 20 July 2022 for the named geographical areas. The colored bars indicate the normalized residence time over a certain region of an air mass at a certain arrival height.

and approximately the same time over continental Europe. With these details, the path of this layer's air mass could be reconstructed. The Saharan air mass crossed the Iberian Peninsula and became mixed with smoke particles from the wildfires in Portugal and Spain. On its further way over the Atlantic Ocean, some aging could take place until it arrived at Leipzig. All in all, it leads to the conclusion that the observed aerosol layer 2 was a mixture of aged wildfire smoke particles from the Iberian Peninsula and Saharan dust particles.

In the altitude range of layer 1, the air-mass-source tool calculated only smaller residence times below 5 km. At 4.5 km altitude, the normalized residence time over the Sahara was below 7 %. At a height of 5 km, the residence time below the reception height was already negligible. Hence, there may still have been some dust particles in layer 1, but all in all, this layer was more dominated by pure wildfire smoke.

To obtain a detailed quantitative view on the observed aerosol layers, 2-hour-mean height profiles of the backscatter coefficients and the fluorescence capacity from 20:50 to 22:50 UTC on 19 July 2022 and 1-hour-mean height profiles of the same quantities from 01:15 to 02:15 UTC on 20 July 2022 are displayed in Fig. 5.9. The dust-smoke mixture in layer 2 showed a fluorescence capacity of around 4.7×10^{-5} at 3 km height (cf. Fig. 5.9(b)). In layer 1, the 532 nm particle backscatter coefficient ($\beta_{532}^{\mathrm{NR}} \approx 1.45\,\mathrm{Mm}^{-1}\,\mathrm{sr}^{-1}$) was exactly four orders of magnitude larger than β_{Fluo}. This resulted in a corresponding fluorescence capacity of about 1×10^{-4} (cf. Fig. 5.9(a)).

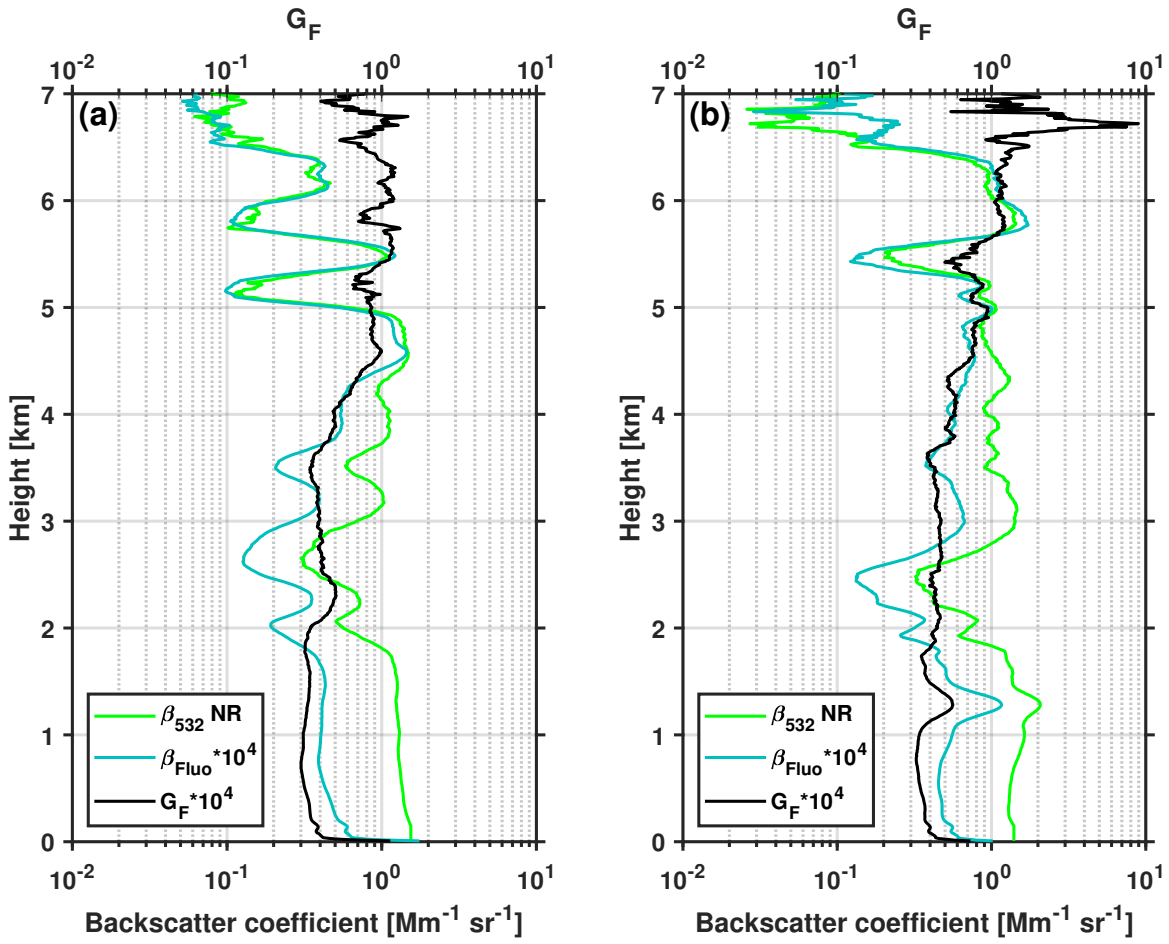

Figure 5.9: Vertical profiles of aerosol ($\beta_{532}^{\mathrm{NR}}$) and fluorescence backscatter coefficients (β_{Fluo}) together with the fluorescence capacity (G_{F}): (a) for the period from 20:50−22:50 UTC on 19 July 2022 and (b) for the period from 01:15−02:15 UTC on 20 July 2022.

5.3.2 Pure smoke (layer 3)

Another aerosol layer at 5.5 km height (layer 3) reached an even higher fluorescence capacity ($G_{\mathrm{F}} = 1.2 \times 10^{-4}$) than layer 1, although its fluorescence backscatter coefficient ($\beta_{\mathrm{Fluo}} = 1.22 \times 10^{-4}\,\mathrm{Mm^{-1}\,sr^{-1}}$) was slightly lower. I.e., the elastic particle backscatter coefficient of layer 3 was lower ($\beta_{532}^{\mathrm{NR}} \approx 1\,\mathrm{Mm^{-1}\,sr^{-1}}$), indicating a lower aerosol load than in layer 1. Also, the depolarization ratio was very low (cf. Fig. 5.7(c)), and the air-mass-source tool calculated no dust fraction anymore in this layer (cf. Fig. 5.8). Thus, this layer seems to have consisted of pure wildfire smoke. In general, at 5.5 km altitude, no residence time below the reception height was calculated. I.e., this air mass was influenced by long-range transport at altitudes above 5 km. As a result, the contained wildfire smoke had to be entrained at higher altitudes as well. When large wildfires generate strong updrafts, smoke injection heights of up to 5.9 km are possible (Amiridis et al., 2010). Therefore, it can be concluded that layer 3 consisted of pure wildfire smoke that was entrained at altitudes above 5 km.

5.3.3 Smoke from Saxonian wildfires (layer 4)

At the end of this measurement (0:15 to 2:15 UTC), another interesting feature occurred inside the boundary layer. A layer at 1.25 km height appeared with a high signal at 1064 nm and a strong fluorescence backscatter coefficient of about $\beta_{\mathrm{Fluo}} = 1.15 \times 10^{-4}\,\mathrm{Mm^{-1}\,sr^{-1}}$ in the temporal mean and up to $4 \times 10^{-4}\,\mathrm{Mm^{-1}\,sr^{-1}}$ in the maximum (cf. Figs. 5.7(a), 5.9(b) and 5.7(b)). The low altitude of this strongly fluorescing layer points to a local source. Indeed, there were several smaller wildfires active in the forests of Saxony during these days. Fig. 5.10 shows the backward trajectories for several ensemble runs of the HYSPLIT model at 2 UTC on 20 July 2022, for an arrival height of 1.25 km. The locations of three relevant wildfires are marked with colored stars. On 19 July 2022, local fire brigades reported wildfires in the Königsbrucker Heide (yellow star in Fig. 5.10), near Coswig (blue star), and at the Bastei bridge (red star) in the Saxon Switzerland. About half of the calculated trajectories pass over the region around the reported wildfires. Thus, it can be concluded that the strongly fluorescing aerosol layer at the end of the measurement probably contained BBA from one of these wildfires.

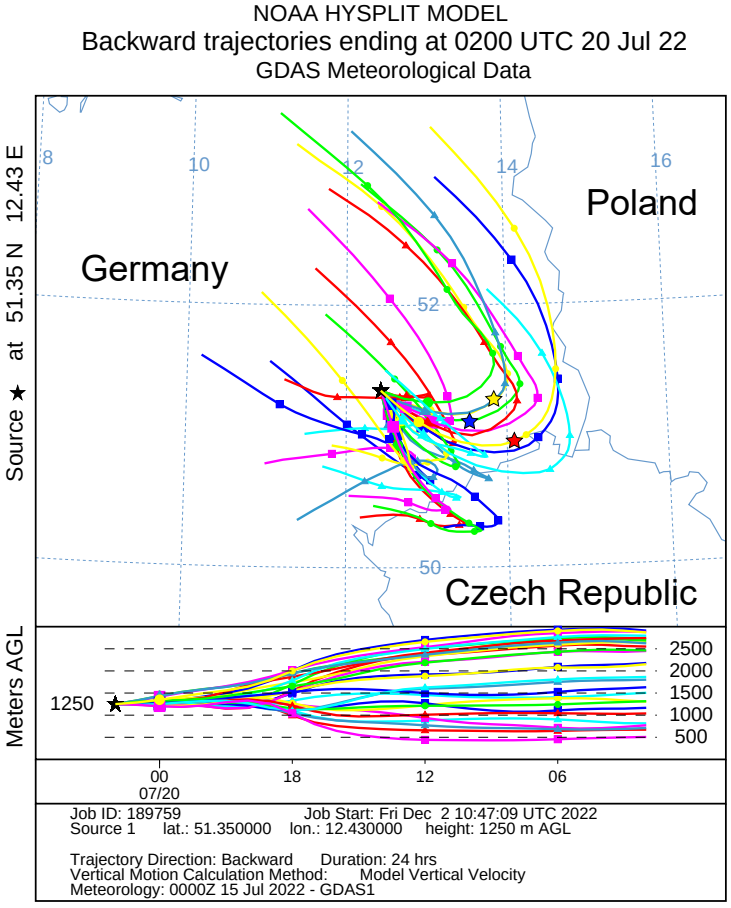

Figure 5.10: HYSPLIT ensemble backward trajectories for an arrival height of 1.25 km at Leipzig at 2 UTC on 20 July 2022. The colored stars indicate the locations of reported local wildfires: Würschnitz (yellow star), Coswig (blue star) and the Bastei bridge (red star).

5.4 Hidden aerosol layers – case of 21 September 2022

As a last example, the first measurement with both the near-range and the far-range fluorescence channels on 21 September 2022 shall be analyzed. The measurement lasted from 19:04 to 23:04 UTC and thus provided 4 hours of measurement. The height-time distribution of the range-corrected signal at 1064 nm measured with the far-range receiver is displayed in Fig. 5.11(a). Based on this, the atmosphere seemed to be quite clean. Enhanced signals were only shown by the boundary layer and a vertically thin cloud at around 4 km height, which was present for less than one hour between 21 and 22 UTC. Also, except for the cloud, the depolarization ratio (not shown) was very low for the whole measurement period.

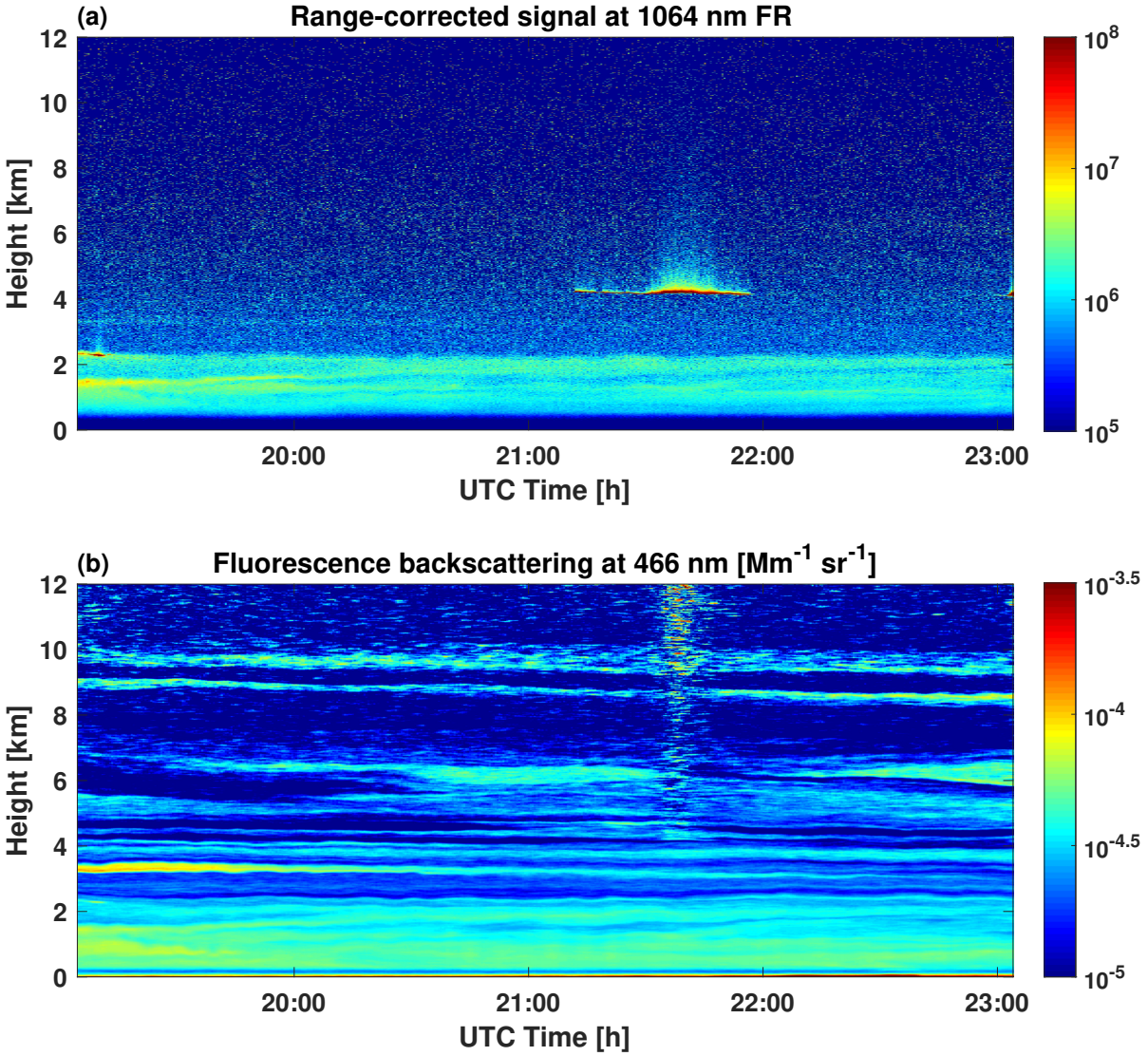

Figure 5.11: Height-time distributions of the (a) range-corrected lidar signal at 1064 nm and (b) fluorescence backscatter coefficient at 466 nm measured with MARTHA at Leipzig on 21 September 2022.

However, a look at the fluorescence backscatter coefficient measured with the far-range receiver in Fig. 5.11(b) draws a completely different picture. Several layers with an enhanced β_{Fluo} (at 3–4, 5, 6.5, 8.5 and 9.5 km) indicate the presence of fluorescing aerosol. This measurement demonstrates quite impressively that we are now able to detect aerosol layers with the new fluorescence channels that we would have missed before with the usual setup only. This fact is also illustrated by the time-averaged vertical profiles of the fluorescence and 532 nm elastic backscatter coefficients and the fluorescence capacity in Fig. 5.12(a). Only the quantities measured with the far-range receiver are shown because the near-range channel probably still had some technical and cross-talk issues. To exclude the cloud, the profiles were only averaged over the time period from 19:04 to 21:04 UTC, before the cloud was present. While the lowest (at 3.3 km altitude) and most fluorescent ($\beta_{\mathrm{Fluo}} = 4 \times 10^{-5}\,\mathrm{Mm^{-1}\,sr^{-1}}$) layer above the boundary layer still showed (albeit only slightly) enhanced elastic backscattering coefficients, the two highest layers (around 8.5 and 9.5 km) had only a weak maximum in β_{532}. In the height range of the mid-level layers (around 5 and 6.5 km altitude), the elastic backscatter coefficients even appeared com-

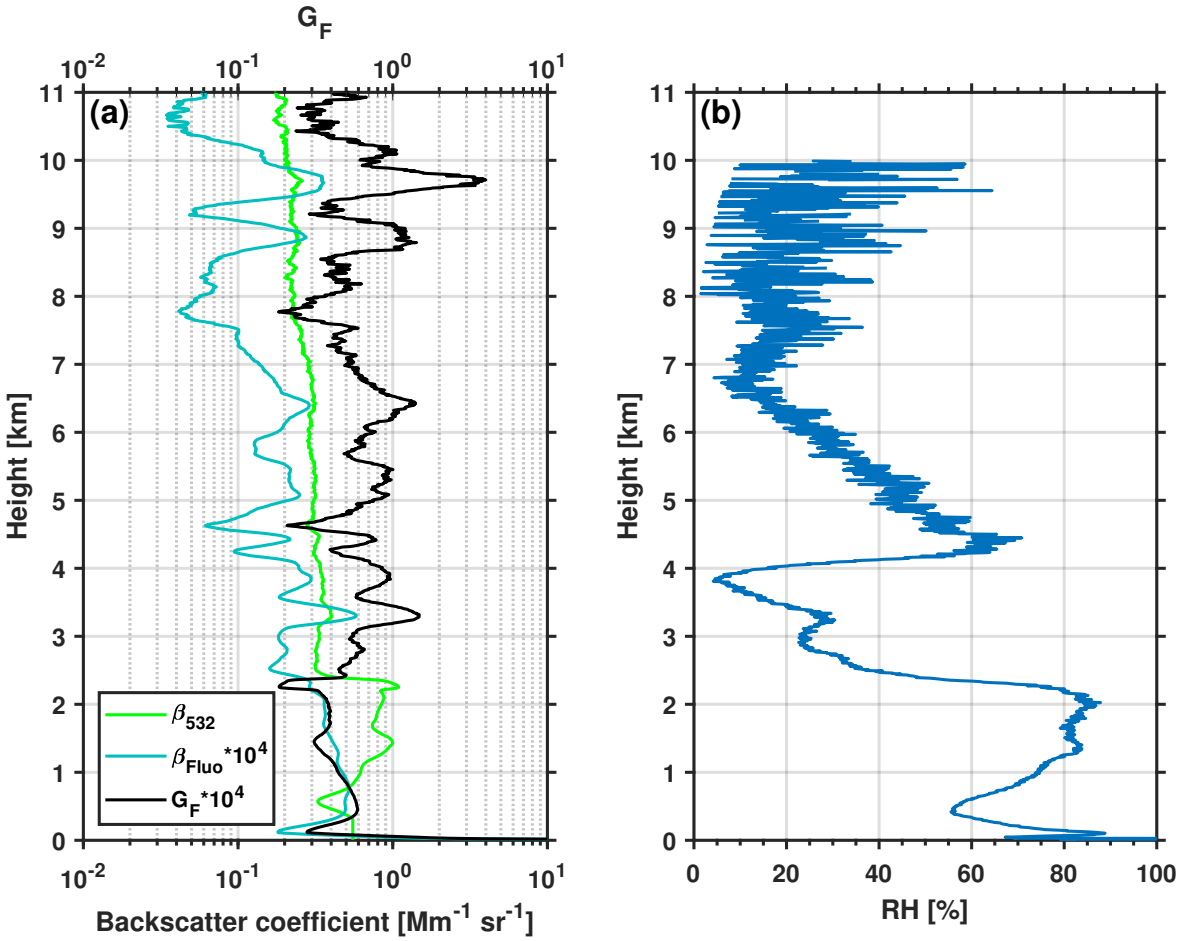

Figure 5.12: Vertical profiles of (a) fluorescence (β_{Fluo}) and elastic backscatter coefficients (β_{532}) together with the fluorescence capacity (G_{F}) and (b) relative humidity averaged over the time period from 19:04–21:04 UTC on 21 September 2022.

pletely unimpressed for this averaging period. Only when looking at them for a shorter averaging period of one hour, keeping the two layers approximately constant in altitude, β_{1064} and β_{355} showed weak maxima, but with a rather low signal-to-noise ratio.
Again, most of the observed fluorescing aerosol layers were very dry. The vertical profile of the time-averaged relative humidity is shown in Fig. 5.12(b). In the height range of the lowest layer below 4 km the RH was below 10 %, the layer around 6.5 km height showed about 10 % RH. Also in the two higher layers it was < 20 %. Even the most humid layer (in the height range of the cloud) did not exceed 70 % RH.
In summary, aerosol layers that previously could only be detected by smart time averaging of the vertical profiles of the elastic backscatter coefficients are now already visible in the signal plots of the new far-range fluorescence channel. This is an important step forward towards the overall goal of being able to detect also uncommon aerosol layers of biological origin.

5.5 Statistics

Finally, a more general view on the first measurements with the new far-range fluorescence channel of MARTHA shall be provided. Although until now only a few measurements have been conducted, Figs. 5.13 and 5.14 present statistics of the fluorescence backscatter coefficient, fluorescence capacity and particle depolarization ratio for the aerosol layers observed during 12 measurements with the far-range fluorescence channel since 1 August 2022. For each measurement case, the aerosol layers of interest were selected manually. For one data point, the temporal mean of the respective quantity over a time period of 30 minutes was calculated at the center of the layer. A total of 41 time frames from various fluorescent aerosol layers were selected and analyzed.
For an overview of the orders of magnitude in which they range, the fluorescence backscatter coefficient is plotted versus the fluorescence capacity in Fig. 5.13. In general, β_{Fluo} ranges between $1 \times 10^{-5}\,\mathrm{Mm^{-1}\,sr^{-1}}$ and $3.5 \times 10^{-4}\,\mathrm{Mm^{-1}\,sr^{-1}}$, i.e., it is about four orders of magnitude smaller than the elastic backscatter coefficients, in agreement with the findings by Veselovskii et al. (2020). Thereby, most (59 %) of the measurement points are in

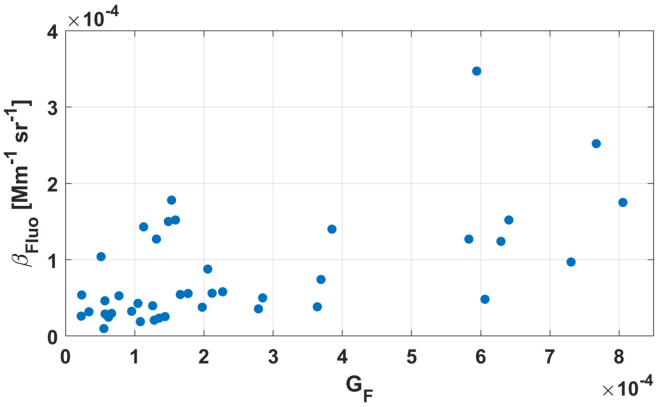

Figure 5.13: Fluorescence backscatter coefficient versus the fluorescence capacity for the measurements with the far-range fluorescence channel.

the range of $2{-}6 \times 10^{-5}\,\mathrm{Mm^{-1}\,sr^{-1}}$. Almost one third (32 %) of the selected layers had a fluorescence backscatter coefficient of $> 10^{-4}\,\mathrm{Mm^{-1}\,sr^{-1}}$, whereas only two data points also exceeded a threshold of $2 \times 10^{-4}\,\mathrm{Mm^{-1}\,sr^{-1}}$. The fluorescence capacity varies between 2×10^{-5} and 8×10^{-4}. However, more than two thirds (68 %) of the data points are below $G_\mathrm{F} = 2.5 \times 10^{-4}$. Eight out of the 41 measurement points ($\approx 19.5\,\%$) show a significantly higher fluorescence capacity of $> 5.5 \times 10^{-4}$ compared to the rest. These values are higher than the maximum values of $G_\mathrm{F} = 1{-}5 \times 10^{-4}$ found by Veselovskii et al. (2021, 2022a) and Hu et al. (2022) for wildfire smoke layers.

To use the new fluorescence quantities for an improvement of the aerosol classification, one has to combine their information with other lidar-relevant quantities. Therefore, the 532 nm particle depolarization ratio measured by Polly$^{\mathrm{XT}}$ is plotted against the fluorescence capacity determined with MARTHA in Fig. 5.14. Even with this small number of data points, single clusters already form. First, there is the cluster of weakly fluorescing aerosol layers with enhanced depolarization ratios (orange ellipse in Fig. 5.14). Four data points exhibit 532 nm particle depolarization ratios of 6.5 % to 8.5 % and another one even reaches nearly 13 %, while the rest shows values below 4 %. Weak fluorescence combined with enhanced depolarization indicates desert dust (cf. Tab. 2.1). As pure dust typically shows even higher depolarization ratios of $\delta_\mathrm{par} > 20\,\%$ (Freudenthaler et al., 2009; Groß et al., 2011; Haarig et al., 2017; Floutsi et al., 2022), these layers were probably dust-dominated mixtures. A second cluster is formed by layers with strong fluorescence and rather low depolarization ratios (black ellipse in Fig. 5.14). High fluorescence capacities of $> 5.5 \times 10^{-4}$ combined with low depolarization ratios (mainly below 2 %) indicate long-range-transported and aged wildfire smoke. As a third cluster, the data points with rather low depolarization ($\delta_\mathrm{par} < 4\,\%$) and fluorescence capacity ($G_\mathrm{F} < 2.5 \times 10^{-4}$) can be grouped. Looking at the measurement height, it can be seen that most of these aerosol layers were located below 2 km altitude, up to where the atmospheric boundary layer typically reached. Thus, it can be concluded that this cluster is representative for boundary-layer aerosol. This analysis demonstrates impressively that the combination of fluorescence and depolarization has a great potential to improve the aerosol classification by lidar measurements.

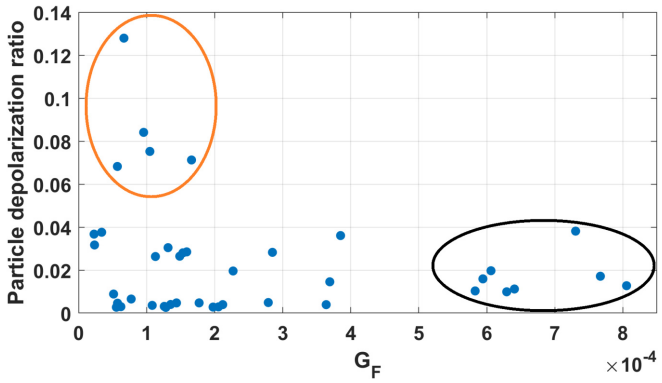

Figure 5.14: 532 nm particle depolarization ratio versus the fluorescence capacity for the measurements with the far-range fluorescence channel.

6 Conclusion and outlook

In this Master project, the MARTHA lidar system at TROPOS was upgraded by implementing a new fluorescence channel into both the near-range and far-range receivers. Two identical interference filters in tandem, centered at 466 nm and with a width of 44 nm, select a part of the fluorescence spectrum of fluorescing atmospheric particles and at the same time strongly suppress the elastic backscattering at the three laser wavelengths. A calculation approach for the fluorescence backscatter coefficient, inspired by Veselovskii et al. (2020), was developed and further improved. As this approach uses a calibrated ratio of the fluorescence channel's signal and the nitrogen Raman signal, no reference height is needed to determine β_{Fluo}. Three measurement cases from summer and early autumn 2022 demonstrated the benefits of the new fluorescence information.

Already the measurements with the near-range channel, which was installed first due to delivery delays, showed that with this filter approach it is possible to detect the fluorescence of aerosol layers in the lower and middle troposphere. The analysis confirmed the size range of β_{Fluo} as four orders of magnitude lower than the elastic backscatter coefficients, as stated by Veselovskii et al. (2020). Especially the data of a major smoke event in the middle of July 2022 were very enlightening. β_{Fluo} varied from $0.26 \times 10^{-4}\,\mathrm{Mm^{-1}\,sr^{-1}}$ for boundary-layer aerosol up to $1.45 \times 10^{-4}\,\mathrm{Mm^{-1}\,sr^{-1}}$ for a strong smoke layer. The fluorescence capacity proved to be a useful tool to separate clouds ($G_{\mathrm{F}} < 5 \times 10^{-6}$) from fluorescent aerosol. Moreover, when comparing two layers in combination with the associated elastic backscatter coefficients, G_{F} is a first indication of the fraction of fluorescent particles in the respective aerosol layer.

The far-range fluorescence channel was even capable of detecting thin smoke layers ($\beta_{1064} < 0.05\,\mathrm{Mm^{-1}\,sr^{-1}}$) in the upper troposphere and lower stratosphere up to 14 km height. Here, β_{Fluo} ranged between $1 \times 10^{-5}\,\mathrm{Mm^{-1}\,sr^{-1}}$ and $3.5 \times 10^{-4}\,\mathrm{Mm^{-1}\,sr^{-1}}$, with the low values belonging to dust (mixtures) and the higher values to smoke layers of wildfires. Particularly outstanding is that some of these fluorescent layers were not detectable in the range-corrected signals of the elastic channels. This important finding is a step forward towards the goal of detecting traces of biological particles in the atmosphere.

A first statistical evaluation of the measurements with the far-range fluorescence channel indicated a fluorescence backscatter coefficient in the range of $2{-}6 \times 10^{-5}\,\mathrm{Mm^{-1}\,sr^{-1}}$ for most aerosol layers. The fluorescence capacity varied between 2×10^{-5} and 8×10^{-4}, and the smoke layers were characterized by significantly higher values than the rest. In contrast, the dust mixtures showed rather low values of G_{F}. This characteristic emphasizes the fluorescence capacity's potential for aerosol classification, particularly when combined with depolarization.

As the water-vapor channel was kept in the new MARTHA setup, the relative-humidity information could be used to show that most of the observed fluorescing aerosol layers were very dry. This anti-correlation of fluorescence and water vapor is an interesting issue to investigate and should therefore be considered further in future research.

Another challenge for the future is the design of a second fluorescence channel in the spectral range $> 500\,\mathrm{nm}$, which can detect the part of the spectrum where the fluorescence of wildfire smoke reaches its maximum. Such a setup would allow a direct distinction of pollen and smoke by building the ratio of both fluorescence channels. Moreover, the use of a spectrometer for continuous spectral information is a promising option for further development of fluorescence techniques in MARTHA. There is also the potential to implement a fluorescence channel into a portable lidar system, allowing us to ship it to places where large amounts of fluorescing aerosols are present and can be explored by fluorescence lidar.

A Solution of the lidar equation

This section is based on the description of the Raman and Klett retrieval methods, recently summarized by Jiménez (2021). Considering the molecular and particulate components of extinction and backscatter coefficient (Eqs. (2.5) and (2.8)), Eq. (2.9) can be written in the form

$$P(R,\lambda) = P_0 \frac{c\tau}{2} A\eta \frac{O(R)}{R^2} [\beta_{\mathrm{mol}}(R,\lambda) + \beta_{\mathrm{par}}(R,\lambda)] \exp\left[-2\int_0^R [\alpha_{\mathrm{mol}}(r,\lambda) + \alpha_{\mathrm{par}}(r,\lambda)]\mathrm{d}r\right]. \tag{A.1}$$

The molecular extinction and backscatter coefficient can be combined to the molecular lidar ratio (Collis and Russell, 1976):

$$S_{\mathrm{mol}} = \frac{\alpha_{\mathrm{mol}}}{\beta_{\mathrm{mol}}} = \frac{8\pi}{3} K, \tag{A.2}$$

with the King's factor K describing the air molecules' anisotropy. Still, $\alpha_{\mathrm{par}}(r,\lambda)$, $\beta_{\mathrm{par}}(r,\lambda)$ and $O(R)$ remain as unknowns in the lidar equation. Depending on the lidar type and measuring time, the Raman and/or the Klett method can be used to solve it. Both retrievals are described in the next subsections.

A.1 Raman method

Eqs. (2.10) and (2.11) for the nitrogen Raman signal were already introduced in Sec. 2.2. An expression for the Raman backscatter coefficient of nitrogen molecules was given in Eq. (3.22). As D_{R} and D_{mol} are constant, the expression

$$C^*_{\lambda_{\mathrm{Ra}}} = 0.78 \frac{D_{\mathrm{R}}}{D_{\mathrm{mol}}} P_0 \frac{c\tau}{2} A\eta \tag{A.3}$$

defines a new constant. Then, Eq. (2.10) can be rewritten as the range-corrected and overlap-corrected signal $P_{\mathrm{RC}}(R,\lambda_{\mathrm{Ra}})$:

$$P_{\mathrm{RC}}(R,\lambda_{\mathrm{Ra}}) = P(R,\lambda_{\mathrm{Ra}}) \frac{R^2}{O(R)} = C^*_{\lambda_{\mathrm{Ra}}} \beta_{\mathrm{mol}}(R,\lambda_0) \exp\left[-\int_0^R [\alpha(r,\lambda_0) + \alpha(r,\lambda_{\mathrm{Ra}})]\mathrm{d}r\right]. \tag{A.4}$$

After some transformation steps, Ansmann et al. (1990) found a solution for the particle extinction coefficient:

$$\alpha_{\mathrm{par}}(R,\lambda_0) = \frac{\frac{\mathrm{d}}{\mathrm{dz}} \ln \frac{\beta_{\mathrm{mol}}(R,\lambda_0)}{P_{\mathrm{RC}}(R,\lambda_{\mathrm{Ra}})} - \alpha_{\mathrm{mol}}(R,\lambda_0) - \alpha_{\mathrm{mol}}(R,\lambda_{\mathrm{Ra}})}{1 + \left(\frac{\lambda_0}{\lambda_{\mathrm{Ra}}}\right)^{\mathring{a}}}. \tag{A.5}$$

å is the Ångström exponent, which describes the spectral dependency of the aerosol properties and is defined by Ångström (1964):

$$\frac{\alpha_{\mathrm{par}}(R,\lambda_{\mathrm{Ra}})}{\alpha_{\mathrm{par}}(R,\lambda_0)} = \left(\frac{\lambda_0}{\lambda_{\mathrm{Ra}}}\right)^{\text{å}}. \tag{A.6}$$

In a next step, Eq. (A.1) is divided by Eq. (A.4):

$$\begin{aligned}\frac{P(R,\lambda_0)}{P(R,\lambda_{\mathrm{Ra}})} = \frac{C_{\lambda_0}}{C^*_{\lambda_{\mathrm{Ra}}}} \frac{\beta_{\mathrm{par}}(R,\lambda_0)+\beta_{\mathrm{mol}}(R,\lambda_0)}{\beta_{\mathrm{mol}}(R,\lambda_0)} \\ \times \exp\left[-\int_0^R [\alpha_{\mathrm{mol}}(r,\lambda_0)-\alpha_{\mathrm{mol}}(r,\lambda_{\mathrm{Ra}})+\alpha_{\mathrm{par}}(r,\lambda_0)-\alpha_{\mathrm{par}}(r,\lambda_{\mathrm{Ra}})]\mathrm{d}r\right],\end{aligned} \tag{A.7}$$

with the lidar constant $C_{\lambda_0} = P_0 \frac{c\tau}{2} A\eta$. It is necessary to choose a reference height R_0 (usually somewhere in the upper troposphere), where the particle influence can be neglected ($\beta_{\mathrm{par}}(R_0,\lambda_0) + \beta_{\mathrm{mol}}(R_0,\lambda_0) \approxeq \beta_{\mathrm{mol}}(R_0,\lambda_0)$). The profiles of the molecular extinction and backscatter coefficients can be derived from atmospheric temperature and pressure profiles. Then, the particle backscatter coefficient can be calculated with the following equation (Ansmann et al., 1992):

$$\begin{aligned}\beta_{\mathrm{par}}(R,\lambda_0) = [\beta_{\mathrm{par}}(R_0,\lambda_0)+\beta_{\mathrm{mol}}(R_0,\lambda_0)] \frac{P(R_0,\lambda_{\mathrm{Ra}})P(R,\lambda_0)N_{\mathrm{N_2}}(R)}{P(R_0,\lambda_0)P(R,\lambda_{\mathrm{Ra}})N_{\mathrm{N_2}}(R_0)} \\ \times \frac{\exp\left[-\int_{R_0}^R [\alpha_{\mathrm{par}}(r,\lambda_{\mathrm{Ra}})+\alpha_{\mathrm{mol}}(r,\lambda_{\mathrm{Ra}})]\mathrm{d}r\right]}{\exp\left[-\int_{R_0}^R [\alpha_{\mathrm{par}}(r,\lambda_0)+\alpha_{\mathrm{mol}}(r,\lambda_0)]\mathrm{d}r\right]} - \beta_{\mathrm{mol}}(R,\lambda_0).\end{aligned} \tag{A.8}$$

With Eqs. (A.5) and (A.8) the extinction and backscatter coefficients can be derived independently and accurately. The overlap function has to be known for the calculation of $\alpha_{\mathrm{par}}(R,\lambda_0)$.

A.2 Klett method

The Raman method represents a robust solution to retrieve both extinction and backscatter coefficients independently. Unfortunately, during daytime the sky background is too large, so that the Raman channels are considerably noisy. In this case, the Klett solution is applied to the elastic lidar signals only.

In the elastic lidar equation (Eq. (A.1)), the lidar constant and the particle extinction and backscatter coefficients remain unknown. As only an elastic signal is available, additional information is needed. Therefore, the lidar ratio $S_{\mathrm{par}}(\lambda_0)$, which relates the aerosol extinction and backscatter coefficient (cf. Eq. (2.12)), is assumed as vertically constant. With this assumption, Klett (1981) derived a solution for only one type of scatterer, while Fernald (1984) generalized it for an atmosphere consisting of molecules and particles. The

particle backscatter coefficient is then calculated as

$$\beta_{\mathrm{par}}(R,\lambda_0) = \frac{U(R_0,R)}{V(R_0) - 2S_{\mathrm{par}}(\lambda_0)\int_{R_0}^{R} U(R_0,r)\mathrm{d}r} - \beta_{\mathrm{mol}}(R,\lambda_0), \tag{A.9}$$

with

$$U(R_0,R) = P(R,\lambda_0)R^2 \exp\left[-2[S_{\mathrm{par}}(\lambda_0) - S_{\mathrm{mol}}]\int_{R_0}^{R}\beta_{\mathrm{mol}}(r,\lambda_0)\mathrm{d}r\right] \tag{A.10}$$

and

$$V(R_0) = \frac{P(R_0,\lambda_0)R_0^2}{\beta_{\mathrm{par}}(R_0,\lambda_0) + \beta_{\mathrm{mol}}(R_0,\lambda_0)}. \tag{A.11}$$

Again, the reference height R_0 is chosen in a way that the particle backscatter coefficient in this height can be assumed as zero. $\beta_{\mathrm{mol}}(R,\lambda_0)$ can be derived from atmospheric temperature and pressure profiles. In addition, a proper value for $S_{\mathrm{par}}(\lambda_0)$ must be assumed. In summary, the Klett retrieval impresses on the one hand with a high spatial and temporal resolution and can also be applied during daytime. On the other hand, a vertically constant lidar ratio has to be assumed, resulting in the problem that the lidar ratio is not an independent variable for the aerosol typing (see Sec. 2.4) anymore. Systematic errors are made, and the solution is stable only for backward integrals (Jiménez, 2021).

B Additional tools and auxiliary data

B.1 ZEMAX

For the geometrical design of the new fluorescence channels, an existing optical model of the MARTHA system was supplemented using the ZEMAX program. ZEMAX supports the design of an optical system by modeling and analysis tools. It allows us to simulate and optimize the performance of an optical system by offering multiple ray-tracing options (ZEMAX, 2005).

First, the optical components needed for the fluorescence channels were inserted into the program and given the appropriate optical properties. This was done by combining several surfaces with certain radius of curvature, thickness and glass type. If necessary, a coating could be added to a surface additionally. Then, the distances between the optical elements were adjusted in order to produce a sharp image on the detector at the end of the channel. The result is shown in the optical setup of the new far-range fluorescence channel in Fig. 4.10.

B.2 HYSPLIT

The HYbrid Single-Particle Lagrangian Integrated Trajectory model (HYSPLIT) of the National Oceanic and Atmospheric Administration (NOAA) Air Resources Laboratory (ARL) can be used for simple applications like the computation of air-parcel trajectories, but it can also perform more complex simulations of aerosol transport, dispersion, chemical transformation and deposition (Stein et al., 2015). HYSPLIT combines the Lagrangian and the Eulerian approach. For advection and diffusion calculations, a moving Lagrangian framework of reference is used, following the transport path of the considered air parcels from their initial location. The air concentration of a pollutant is computed on a fixed three-dimensional (3D) grid (Stein et al., 2015). Initially, a single pollutant particle is considered as the source. To account for its dispersion by the complex wind field, the initial particle is divided into multiple particles, which spread from the source region in different wind directions (Draxler, 1992).
In this Master thesis, HYSPLIT was used for the most common calculation of back-trajectories in order to attribute a source region to an observed aerosol event. The trajectory of an air parcel is computed from its advection by the wind field. If the calculated path exits the top of the model, the trajectory is terminated. In contrast, the trajectory is continued when it reaches the ground (Draxler and Hess, 1998).

B.3 Polly^{XT}

In addition to MARTHA, a continuously and autonomously measuring lidar, Polly^{XT}, was used for comparison and additional information. It is located at the same measuring site as the MARTHA system, making it well suited for comparison and synergy effects. Polly^{XT} has been used in worldwide field campaigns on land sites as well as aboard the research vessels *Polarstern*, *Meteor* and *Sonne* (Engelmann et al., 2016). The Polly^{XT} systems, developed and built at TROPOS, allow the observation of backscatter coefficients at three wavelengths (355, 532 and 1064 nm), extinction coefficients and depolarization ratios at two wavelengths (355 and 532 nm) and water vapor in the far range (30 cm telescope diameter). In addition, two backscatter and extinction coefficients (355 and 532 nm) are determined in the near range (5 cm telescope). The near-range receiver enables one to reach lower measurement heights in the planetary boundary layer, down to 120 m above the lidar (Engelmann et al., 2016). In this thesis, Polly^{XT} measurements of the depolarization ratio are used.

B.4 MODIS Fire and Thermal Anomalies product

When it was suspected that a detected layer originated from wildfires, the **MOD**erate Resolution **I**maging **S**pectroradiometer (MODIS) Fire and Thermal Anomalies product was used for orientation. MODIS is a cross-track scanning radiometer that is mounted aboard the Terra and Aqua satellites. It has the aim of continuously collecting global radiation data. The Terra and Aqua MODIS sensors provide a view of the entire earth's

surface every 1 to 2 days (Xiong and Barnes, 2006).
The 36 spectral bands (20 in the solar and 16 in the thermal wavelength range) allow observations at wavelengths from 0.41 to 14.5 µm and different spatial resolutions of 250 m (bands 1−2), 500 m (bands 3−7) and 1 km (bands 8−36) (Xiong and Barnes, 2006). The MODIS Fire and Thermal Anomalies product is based on an enhanced fire detection algorithm using the brightness temperatures from the 4 and 11 µm channels of MODIS. Besides the absolute fire detection via a threshold in brightness temperature for strong fires, weaker ones can be detected relative to the brightness temperature of surrounding non-fire background pixels (Giglio et al., 2003).

List of Figures

List of Tables

References

Adam, M. (2009). Notes on temperature-dependent lidar equations. *Journal of Atmospheric and Oceanic Technology*, 26(6):1021–1039.

Amiridis, V., Giannakaki, E., Balis, D. S., Gerasopoulos, E., Pytharoulis, I., Zanis, P., Kazadzis, S., Melas, D., and Zerefos, C. (2010). Smoke injection heights from agricultural burning in Eastern Europe as seen by CALIPSO. *Atmospheric Chemistry and Physics*, 10(23):11567–11576.

Ansmann, A. and Müller, D. (2005). Lidar and Atmospheric Aerosol Particles. In Weitkamp, C., editor, *Lidar: Range-Resolved Optical Remote Sensing of the Atmosphere*, pages 105–141. Springer New York.

Ansmann, A., Riebesell, M., and Weitkamp, C. (1990). Measurement of atmospheric aerosol extinction profiles with a Raman lidar. *Optics Letters*, 15(13):746–748.

Ansmann, A., Tesche, M., Groß, S., Freudenthaler, V., Seifert, P., Hiebsch, A., Schmidt, J., Wandinger, U., Mattis, I., Müller, D., and Wiegner, M. (2010). The 16 April 2010 major volcanic ash plume over central Europe: EARLINET lidar and AERONET photometer observations at Leipzig and Munich, Germany. *Geophysical Research Letters*, 37(13):L13810.

Ansmann, A., Wandinger, U., Riebesell, M., Weitkamp, C., and Michaelis, W. (1992). Independent measurement of extinction and backscatter profiles in cirrus clouds by using a combined Raman elastic-backscatter lidar. *Applied Optics*, 31(33):7113–7131.

Burton, S. P., Ferrare, R. A., Hostetler, C. A., Hair, J. W., Rogers, R. R., Obland, M. D., Butler, C. F., Cook, A. L., Harper, D. B., and Froyd, K. D. (2012). Aerosol classification using airborne High Spectral Resolution Lidar measurements – methodology and examples. *Atmospheric Measurement Techniques*, 5(1):73–98.

Bürgler, A., Glick, S., Hartmann, K., and Eeftens, M. (2021). Rationale and design of a panel study investigating six health effects of airborne pollen: The EPOCHAL study. *Frontiers in Public Health*, 9:689248.

Collis, R. T. H. and Russell, P. B. (1976). Lidar measurement of particles and gases by elastic backscattering and differential absorption. In Hinkley, E. D., editor, *Laser Monitoring of the Atmosphere*, pages 71–151. Springer Berlin Heidelberg.

Damialis, A., Traidl-Hoffmann, C., and Treudler, R. (2019). Climate change and pollen allergies. In Marselle, M. R., Stadler, J., Korn, H., Irvine, K. N., and Bonn, A., editors, *Biodiversity and health in the face of climate change*, pages 47–66. Springer, Cham.

Draxler, R. R. (1992). *Hybrid single-particle Lagrangian integrated trajectories (HYSPLIT), Version 3.0: User's guide and model description.* US Department of Commerce, National Oceanic and Atmospheric Administration, Environmental Research Laboratories, Air Resources Laboratory.

Draxler, R. R. and Hess, G. (1998). An overview of the HYSPLIT_4 modelling system for trajectories. *Australian Meteorological Magazine*, 47(4):295–308.

Engelmann, R., Ansmann, A., Ohneiser, K., Griesche, H., Radenz, M., Hofer, J., Althausen, D., Dahlke, S., Maturilli, M., Veselovskii, I., Jimenez, C., Wiesen, R., Baars, H., Bühl, J., Gebauer, H., Haarig, M., Seifert, P., Wandinger, U., and Macke, A. (2021). Wildfire smoke, Arctic haze, and aerosol effects on mixed-phase and cirrus clouds over the North Pole region during MOSAiC: an introduction. *Atmospheric Chemistry and Physics*, 21(17):13397–13423.

Engelmann, R., Kanitz, T., Baars, H., Heese, B., Althausen, D., Skupin, A., Wandinger, U., Komppula, M., Stachlewska, I. S., Amiridis, V., Marinou, E., Mattis, I., Linné, H., and Ansmann, A. (2016). The automated multiwavelength Raman polarization and water-vapor lidar Polly^{XT}: the neXT generation. *Atmospheric Measurement Techniques*, 9(4):1767–1784.

Fernald, F. G. (1984). Analysis of atmospheric lidar observations: some comments. *Applied Optics*, 23(5):652–653.

Floutsi, A. A., Baars, H., Engelmann, R., Althausen, D., Ansmann, A., Bohlmann, S., Heese, B., Hofer, J., Kanitz, T., Haarig, M., Ohneiser, K., Radenz, M., Seifert, P., Skupin, A., Yin, Z., Abdullaev, S. F., Komppula, M., Filioglou, M., Giannakaki, E., Stachlewska, I. S., Janicka, L., Bortoli, D., Marinou, E., Amiridis, V., Gialitaki, A., Mamouri, R.-E., Barja, B., and Wandinger, U. (2022). DeLiAn – a growing collection of depolarization ratio, lidar ratio and Ångström exponent for different aerosol types and mixtures from ground-based lidar observations. *Atmospheric Measurement Techniques Discussions*, 2022:1–39.

Freudenthaler, V., Esselborn, M., Wiegner, M., Heese, B., Tesche, M., Ansmann, A., Müller, D., Althausen, D., Wirth, M., Fix, A., Ehret, G., Knippertz, P., Toledano, C., Gasteiger, J., Garhammer, M., and Seefeldner, M. (2009). Depolarization ratio profiling at several wavelengths in pure Saharan dust during SAMUM 2006. *Tellus B: Chemical and Physical Meteorology*, 61(1):165–179.

Giglio, L., Descloitres, J., Justice, C. O., and Kaufman, Y. J. (2003). An Enhanced Contextual Fire Detection Algorithm for MODIS. *Remote Sensing of Environment*, 87(2):273–282.

Groß, S., Esselborn, M., Weinzierl, B., Wirth, M., Fix, A., and Petzold, A. (2013). Aerosol classification by airborne high spectral resolution lidar observations. *Atmospheric Chemistry and Physics*, 13(5):2487–2505.

Groß, S., Freudenthaler, V., Wiegner, M., Gasteiger, J., Geiß, A., and Schnell, F. (2012). Dual-wavelength linear depolarization ratio of volcanic aerosols: Lidar measurements of the Eyjafjallajökull plume over Maisach, Germany. *Atmospheric Environment*, 48:85–96.

Groß, S., Tesche, M., Freudenthaler, V., Toledano, C., Wiegner, M., Ansmann, A., Althausen, D., and Seefeldner, M. (2011). Characterization of Saharan dust, marine aerosols and mixtures of biomass-burning aerosols and dust by means of multi-wavelength depolarization and Raman lidar measurements during SAMUM 2. *Tellus B: Chemical and Physical Meteorology*, 63(4):706–724.

Gulev, S. K., Thorne, P. W., Ahn, J., Dentener, F. J., Domingues, C. M., Gerland, S., Gong, D., Kaufman, D. S., Nnamchi, H. C., Quaas, J., Rivera, J. A., Sathyendranath, S., Smith, S. L., Trewin, B., von Schuckmann, K., and Vose, R. S. (2021). Changing state of the climate system. In Masson-Delmotte, V., Zhai, P., Pirani, A., Connors, S. L., Péan, C., Berger, S., Caud, N., Chen, Y., Goldfarb, L., Gomis, M. I., Huang, M., Leitzell, K., Lonnoy, E., Matthews, J. B. R., Maycock, T. K., Waterfield, T., Yelekçi, O., Yu, R., and Zhou, B., editors, *Climate Change 2021: The Physical Science Basis. Contribution of Working Group I to the Sixth Assessment Report of the Intergovernmental Panel on Climate Change*, pages 287–422. Cambridge University Press.

Haarig, M., Ansmann, A., Althausen, D., Klepel, A., Groß, S., Freudenthaler, V., Toledano, C., Mamouri, R.-E., Farrell, D. A., Prescod, D. A., Marinou, E., Burton, S. P., Gasteiger, J., Engelmann, R., and Baars, H. (2017). Triple-wavelength depolarization-ratio profiling of Saharan dust over Barbados during SALTRACE in 2013 and 2014. *Atmospheric Chemistry and Physics*, 17(17):10767–10794.

Haarig, M., Ansmann, A., Baars, H., Jimenez, C., Veselovskii, I., Engelmann, R., and Althausen, D. (2018). Depolarization and lidar ratios at 355, 532, and 1064 nm and microphysical properties of aged tropospheric and stratospheric Canadian wildfire smoke. *Atmospheric Chemistry and Physics*, 18(16):11847–11861.

Haarig, M., Ansmann, A., Engelmann, R., Baars, H., Toledano, C., Torres, B., Althausen, D., Radenz, M., and Wandinger, U. (2022). First triple-wavelength lidar observations of depolarization and extinction-to-backscatter ratios of Saharan dust. *Atmospheric Chemistry and Physics*, 22(1):355–369.

Hu, Q., Goloub, P., Veselovskii, I., and Podvin, T. (2022). The characterization of long-range transported North American biomass burning plumes: what can a multi-wavelength Mie-Raman-polarization-fluorescence lidar provide? *Atmospheric Chemistry and Physics*, 22(8):5399–5414.

Hu, Q., Wang, H., Goloub, P., Li, Z., Veselovskii, I., Podvin, T., Li, K., and Korenskiy, M. (2020). The characterization of Taklamakan dust properties using a multiwave-

length Raman polarization lidar in Kashi, China. *Atmospheric Chemistry and Physics*, 20(22):13817–13834.

Jimenez, C., Ansmann, A., Engelmann, R., Donovan, D., Malinka, A., Seifert, P., Wiesen, R., Radenz, M., Yin, Z., Bühl, J., Schmidt, J., Barja, B., and Wandinger, U. (2020). The dual-field-of-view polarization lidar technique: a new concept in monitoring aerosol effects in liquid-water clouds – case studies. *Atmospheric Chemistry and Physics*, 20(23):15265–15284.

Jiménez, C. A. J. (2021). *Observations of aerosol and liquid-water clouds with Dual-Field-of-View Polarization Lidar*. PhD thesis, Leipzig University.

Jones, M. W., Smith, A., Betts, R., Canadell, J. G., Prentice, I. C., and Le Quéré, C. (2020). Climate change increases the risk of wildfires. *Science Brief Review*.

Kanngiesser, F. and Kahnert, M. (2019). Coating material-dependent differences in modelled lidar-measurable quantities for heavily coated soot particles. *Optics Express*, 27(25):36368–36387.

Klett, J. D. (1981). Stable analytical inversion solution for processing lidar returns. *Applied Optics*, 20(2):211–220.

Lakowicz, J. R. (2006). Introduction to Fluorescence. In Lakowicz, J. R., editor, *Topics in Fluorescence Spectroscopy: Principles*, chapter 1, pages 1–26. Springer Science & Business Media, Boston, third edition.

Lleres, D., Swift, S., and Lamond, A. I. (2007). Detecting Protein-Protein Interactions In Vivo with FRET using Multiphoton Fluorescence Lifetime Imaging Microscopy (FLIM). *Current Protocols in Cytometry*, 42:12.10.1–12.10.19.

Mattis, I., Ansmann, A., Müller, D., Wandinger, U., and Althausen, D. (2004). Multiyear aerosol observations with dual-wavelength Raman lidar in the framework of EARLINET. *Journal of Geophysical Research: Atmospheres*, 109(D13):D13203.

Nitschke, M., Simon, D., Dear, K., Venugopal, K., Jersmann, H., and Lyne, K. (2022). Pollen exposure and cardiopulmonary health impacts in Adelaide, South Australia. *International Journal of Environmental Research and Public Health*, 19(15):9093.

Ohneiser, K., Ansmann, A., Baars, H., Seifert, P., Barja, B., Jimenez, C., Radenz, M., Teisseire, A., Floutsi, A., Haarig, M., Foth, A., Chudnovsky, A., Engelmann, R., Zamorano, F., Bühl, J., and Wandinger, U. (2020). Smoke of extreme Australian bushfires observed in the stratosphere over Punta Arenas, Chile, in January 2020: optical thickness, lidar ratios, and depolarization ratios at 355 and 532 nm. *Atmospheric Chemistry and Physics*, 20(13):8003–8015.

Ohneiser, K., Ansmann, A., Chudnovsky, A., Engelmann, R., Ritter, C., Veselovskii, I., Baars, H., Gebauer, H., Griesche, H., Radenz, M., Hofer, J., Althausen, D., Dahlke, S., and Maturilli, M. (2021). The unexpected smoke layer in the High Arctic winter stratosphere during MOSAiC 2019–2020. *Atmospheric Chemistry and Physics*, 21(20):15783–15808.

Ohneiser, K., Ansmann, A., Kaifler, B., Chudnovsky, A., Barja, B., Knopf, D. A., Kaifler, N., Baars, H., Seifert, P., Villanueva, D., Jimenez, C., Radenz, M., Engelmann, R., Veselovskii, I., and Zamorano, F. (2022). Australian wildfire smoke in the stratosphere: the decay phase in 2020/2021 and impact on ozone depletion. *Atmospheric Chemistry and Physics*, 22(11):7417–7442.

Pan, Y.-L. (2015). Detection and characterization of biological and other organic-carbon aerosol particles in atmosphere using fluorescence. *Journal of Quantitative Spectroscopy and Radiative Transfer*, 150:12–35.

Pan, Y.-L., Hill, S. C., Pinnick, R. G., House, J. M., Flagan, R. C., and Chang, R. K. (2011). Dual-excitation-wavelength fluorescence spectra and elastic scattering for differentiation of single airborne pollen and fungal particles. *Atmospheric Environment*, 45(8):1555–1563.

Radenz, M., Seifert, P., Baars, H., Floutsi, A. A., Yin, Z., and Bühl, J. (2021). Automated time-height-resolved air mass source attribution for profiling remote sensing applications. *Atmospheric Chemistry and Physics*, 21(4):3015–3033.

Reichardt, J., Leinweber, R., and Schwebe, A. (2018). Fluorescing aerosols and clouds: investigations of co-existence. *EPJ Web Conferences*, 176:05010. The 28th International Laser Radar Conference (ILRC 28).

Saito, Y., Ichihara, K., Morishita, K., Uchiyama, K., Kobayashi, F., and Tomida, T. (2018). Remote detection of the fluorescence spectrum of natural pollens floating in the atmosphere using a Laser-Induced-Fluorescence Spectrum (LIFS) lidar. *Remote Sensing*, 10(10):1533.

Sassen, K., Zhu, J., Webley, P., Dean, K., and Cobb, P. (2007). Volcanic ash plume identification using polarization lidar: Augustine eruption, Alaska. *Geophysical Research Letters*, 34(8):L08803.

Schmidt, J., Wandinger, U., and Malinka, A. (2013). Dual-field-of-view Raman lidar measurements for the retrieval of cloud microphysical properties. *Applied Optics*, 52(11):2235–2247.

Stein, A., Draxler, R. R., Rolph, G. D., Stunder, B. J., Cohen, M., and Ngan, F. (2015). NOAA's HYSPLIT atmospheric transport and dispersion modeling system. *Bulletin of the American Meteorological Society*, 96(12):2059–2077.

Veselovskii, I., Goloub, P., Podvin, T., Bovchaliuk, V., Derimian, Y., Augustin, P., Fourmentin, M., Tanre, D., Korenskiy, M., Whiteman, D. N., Diallo, A., Ndiaye, T., Kolgotin, A., and Dubovik, O. (2016). Retrieval of optical and physical properties of African dust from multiwavelength Raman lidar measurements during the SHADOW campaign in Senegal. *Atmospheric Chemistry and Physics*, 16(11):7013–7028.

Veselovskii, I., Hu, Q., Ansmann, A., Goloub, P., Podvin, T., and Korenskiy, M. (2022a). Fluorescence lidar observations of wildfire smoke inside cirrus: a contribution to smoke–cirrus interaction research. *Atmospheric Chemistry and Physics*, 22(8):5209–5221.

Veselovskii, I., Hu, Q., Goloub, P., Podvin, T., Barchunov, B., and Korenskii, M. (2022b). Combining Mie–Raman and fluorescence observations: a step forward in aerosol classification with lidar technology. *Atmospheric Measurement Techniques*, 15(16):4881–4900.

Veselovskii, I., Hu, Q., Goloub, P., Podvin, T., Choël, M., Visez, N., and Korenskiy, M. (2021). Mie–Raman–fluorescence lidar observations of aerosols during pollen season in the north of France. *Atmospheric Measurement Techniques*, 14(7):4773–4786.

Veselovskii, I., Hu, Q., Goloub, P., Podvin, T., Korenskiy, M., Pujol, O., Dubovik, O., and Lopatin, A. (2020). Combined use of Mie–Raman and fluorescence lidar observations for improving aerosol characterization: feasibility experiment. *Atmospheric Measurement Techniques*, 13(12):6691–6701.

Šaulienė, I., Šukienė, L., Daunys, G., Valiulis, G., Vaitkevičius, L., Matavulj, P., Brdar, S., Panic, M., Sikoparija, B., Clot, B., Crouzy, B., and Sofiev, M. (2019). Automatic pollen recognition with the Rapid-E particle counter: the first-level procedure, experience and next steps. *Atmospheric Measurement Techniques*, 12(6):3435–3452.

Wandinger, U. (2005a). Introduction to Lidar. In Weitkamp, C., editor, *Lidar: Range-Resolved Optical Remote Sensing of the Atmosphere*, pages 1–18. Springer New York.

Wandinger, U. (2005b). Raman Lidar. In Weitkamp, C., editor, *Lidar: Range-Resolved Optical Remote Sensing of the Atmosphere*, pages 241–271. Springer New York.

Whiteman, D. N., Demoz, B., Rush, K., Schwemmer, G., Gentry, B., Girolamo, P. D., Comer, J., Veselovskii, I., Evans, K., Melfi, S. H., Wang, Z., Cadirola, M., Mielke, B., Venable, D., and Hove, T. V. (2006). Raman lidar measurements during the International H_2O Project. Part I: Instrumentation and analysis techniques. *Journal of Atmospheric and Oceanic Technology*, 23(2):157–169.

Whiteman, D. N., Melfi, S. H., and Ferrare, R. A. (1992). Raman lidar system for the measurement of water vapor and aerosols in the Earth's atmosphere. *Applied Optics*, 31(16):3068–3082.

Xiong, X. and Barnes, W. (2006). An overview of MODIS radiometric calibration and characterization. *Advances in Atmospheric Sciences*, 23(1):69–79.

Xu, R., Yu, P., Abramson, M. J., Johnston, F. H., Samet, J. M., Bell, M. L., Haines, A., Ebi, K. L., Li, S., and Guo, Y. (2020). Wildfires, global climate change, and human health. *New England Journal of Medicine*, 383(22):2173–2181.

ZEMAX (2005). ZEMAX Optical Design Program, https://www.zemax.com.

Zhang, M., Su, H., Li, G., Kuhn, U., Li, S., Klimach, T., Hoffmann, T., Fu, P., Pöschl, U., and Cheng, Y. (2021). High-resolution fluorescence spectra of airborne biogenic secondary organic aerosols: Comparisons to primary biological aerosol particles and implications for single-particle measurements. *Environmental Science & Technology*, 55(24):16747–16756.

Zhang, Z., Huang, J., Chen, B., Yi, Y., Liu, J., Bi, J., Zhou, T., Huang, Z., and Chen, S. (2019). Three-year continuous observation of pure and polluted dust aerosols over northwest China using the ground-based lidar and Sun photometer data. *Journal of Geophysical Research: Atmospheres*, 124(2):1118–1131.

Ziello, C., Sparks, T. H., Estrella, N., Belmonte, J., Bergmann, K. C., Bucher, E., Brighetti, M. A., Damialis, A., Detandt, M., Galán, C., Gehrig, R., Grewling, L., Gutiérrez Bustillo, A. M., Hallsdóttir, M., Kockhans-Bieda, M.-C., De Linares, C., Myszkowska, D., Pàldy, A., Sánchez, A., Smith, M., Thibaudon, M., Travaglini, A., Uruska, A., Valencia-Barrera, R. M., Vokou, D., Wachter, R., de Weger, L. A., and Menzel, A. (2012). Changes to airborne pollen counts across Europe. *PLOS ONE*, 7(4):1–8.

Ångström, A. (1964). The parameters of atmospheric turbidity. *Tellus*, 16(1):64–75.

Erklärung zur Masterarbeit

Hiermit versichere ich, die vorliegende Masterarbeit ohne Hilfe Dritter nur mit den angegebenen Quellen und Hilfsmitteln angefertigt zu haben. Alle Stellen, die aus den Quellen entnommen wurden, sind als solche kenntlich gemacht worden. Diese Arbeit hat in gleicher Form noch keiner Prüfungsbehörde vorgelegen.

Leipzig, den 02. Februar 2023

_____

Unterschrift